

OPEN ACCESS

## Non-Radiative Processes in Crystals and in Nanocrystals

To cite this article: J. Collins 2016 *ECS J. Solid State Sci. Technol.* **5** R3170

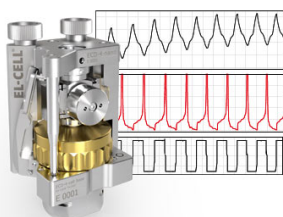
View the [article online](#) for updates and enhancements.

### You may also like

- [Influence of temperature on bandgap shifts, optical properties and photovoltaic parameters of GaAs/AlAs and GaAs/AlSb p-n heterojunctions: insights from \*ab-initio\* DFT + NEGF studies](#)  
Ramesh Mamindla and Manish K Niranjana
- [High-pressure studies with x-rays using diamond anvil cells](#)  
Guoyin Shen and Ho Kwang Mao
- [Phonon thermal conduction in a graphene-C<sub>3</sub>N heterobilayer using molecular dynamics simulations](#)  
Dan Han, Xinyu Wang, Wenyang Ding et al.

### Measure the Electrode Expansion in the Nanometer Range. Discover the new ECD-4-nano!

  
electrochemical test equipment



- Battery Test Cell for Dilatometric Analysis (Expansion of Electrodes)
- Capacitive Displacement Sensor (Range 250  $\mu\text{m}$ , Resolution  $\leq 5$  nm)
- Detect Thickness Changes of the Individual Electrode or the Full Cell.

[www.el-cell.com](http://www.el-cell.com) +49 40 79012-734 [sales@el-cell.com](mailto:sales@el-cell.com)





## Non-Radiative Processes in Crystals and in Nanocrystals

J. Collins<sup>\*,z</sup>

Department of Physics and Astronomy, Wheaton College, Norton, Massachusetts 02766, USA

This paper discusses non-radiative processes that are relevant to the luminescence characteristics of optically active ions doped into insulators or large-gap semiconductors, with particular attention to how these processes are affected as the particle size is reduced from bulk single crystals to as small as a few nanometers. The non-radiative processes discussed in this article are thermal line broadening and thermal line shifting, relaxation via phonons between excited electronic states, vibronic emission and absorption, and phonon-assisted energy transfer. Given that one of the main effects of confinement in these particles is on the phonon density of states, we pay particular attention to how these non-radiative processes are altered due to the change in the phonon density of states as particle size decreases.

© The Author(s) 2015. Published by ECS. This is an open access article distributed under the terms of the Creative Commons Attribution 4.0 License (CC BY, <http://creativecommons.org/licenses/by/4.0/>), which permits unrestricted reuse of the work in any medium, provided the original work is properly cited. [DOI: 10.1149/2.0221601jss] All rights reserved.

Manuscript submitted July 29, 2015; revised manuscript received October 6, 2015. Published October 24, 2015. *This paper is part of the JSS Focus Issue on Novel Applications of Luminescent Optical Materials.*

Inorganic insulators doped with rare-earth ions and transition metal ions represent an important class of luminescent materials for many applications, including phosphors for lighting, scintillators, solid-state laser materials, bio-markers for imaging, and nanothermometry. Following excitation by radiation, the optical ions usually undergo some degree of non-radiative relaxation releasing a part or all of its energy to the lattice. During the non-radiative relaxation, all or part of the electronic energy initially stored in the optically active ion is converted into phonons.

From the perspective of energy efficiency of luminescent materials, it may seem beneficial to attempt to eliminate non-radiative processes altogether. However, the conversion of electronic energy into heat energy following excitation is, in fact, desirable to many applications. Non-radiative processes play an important role in converting light from the blue LED into red and green light for white light generation in lamp phosphors, for efficient operation of many solid-state lasers, for energy transfer and multiphonon relaxation in bio-imaging, and also for the establishment of thermal equilibrium, the principle on which thermometry is based. For these technologies to be optimized, non-radiative processes must be controlled, or at least carefully considered. Thus, understanding these processes is of great interest to the luminescence community. The specific non-radiative processes addressed in this work are thermal line broadening, thermal line shifting, decay via a phonon from one electronic level to another, vibronic transitions, and phonon-assisted energy transfer.

The main focus of this work is on how non-radiative processes are affected as the particle size decreases into the nano-regime. Generally speaking, the two main effects of going from the bulk to the nano are: (1) an increase in the surface to volume ratio, and (2) a reduction in the phonon density of states. Item (1) often leads to an increase in defect sites (mostly near the surface) and surface states, which in turn tends to decrease the luminescence efficiency as one goes from the bulk to the nano. This nonradiative process is outside the scope of this article. Item (2) on the other hand, is a theme that runs throughout this work. Most non-radiative processes that play a significant role in the luminescent properties of these systems involve phonons, and most of those will be, at least in theory, affected by a change in the phonon density of states of the lattice. One goal of this paper is to present results that demonstrate how the reduced density of states in nanoparticles affect the aforementioned processes, and under what conditions will such affects be noticeable.

This work reviews some of the theoretical basis of non-radiative transitions of optically active ions in solids, beginning with the

electron-phonon coupling operator, which couples the electronic motion to the nuclear motion. The systems of primary interest in this paper are those in which this coupling is weak, such as  $f$ - $f$  transitions of rare earth ions and some sharp-line transitions in transition metal ion-doped systems, such as the  ${}^2E$  to  ${}^4T_2$  transition in some Cr-doped oxides.

### Electron-Phonon Coupling

An optically active ion embedded in a solid consists of two subsystems: the electrons and the nuclei. Because the ratio of the nuclear mass to the electronic mass is on the order of  $10^3$ , the nuclei move more slowly than the electrons by a factor of  $10^{-2}$ – $10^{-3}$ . Thus, the electrons and the nuclei constitute a fast subsystem and a slow subsystem, respectively. The formal separation of the electronic and nuclear motions is called the adiabatic approximation, and results in a wavefunction of the system that is a product of an electronic wavefunction,  $\phi_i(r, R)$ , and the nuclear wavefunction,  $\chi_{i,k}(R)$ .

$$\Psi_{i,k}(r, R) = \phi_i(r, R) \chi_{i,k}(R) \quad [1]$$

This is called a Born-Oppenheimer wavefunction. In Equation 1  $r$  represents the positions of the electrons, and  $R$  the nuclear positions. Also, the electronic wavefunction  $\phi_i(r, R)$ , has only a parametric dependence on  $R$ . Treatments in the literature on the adiabatic approximation as applied to molecules or to ions in a solid are plentiful, [e.g. 1 - 9], and so are not discussed here.

Writing the states in the form of Equation 1 is a result of neglecting terms in the Hamiltonian that are responsible for coupling the electronic and nuclear motions. These neglected (non-adiabatic) terms form the electron-phonon coupling operators, which make possible non-radiative decay of an ion from an excited state. The two most commonly used forms of the Adiabatic Approximation are the *Crude Adiabatic Approximation* and the *Born-Oppenheimer Adiabatic Approximation*. Each of these approximations has its own form of the electron-phonon coupling operator, which are now separately discussed.

*Type A electron-phonon coupling.*— In the Crude Adiabatic Approximation, the wavefunctions of an ion in a solid is given by

$$\Psi(r, R) = \phi_k^0(r, R_0) \chi_k(R) \quad [2]$$

where  $R_0$  are the nuclei positions *fixed* at their equilibrium positions when the optically active ion is in its ground state. In arriving at Equation 2, the interaction Hamiltonian between the electrons and nuclei of the system is written in the following form:

$$U(r, R) = U(r, R_0) + \Delta U(r, R) \quad [3]$$

\*Electrochemical Society Active Member.

<sup>z</sup>E-mail: [jcollins@wheatonma.edu](mailto:jcollins@wheatonma.edu)

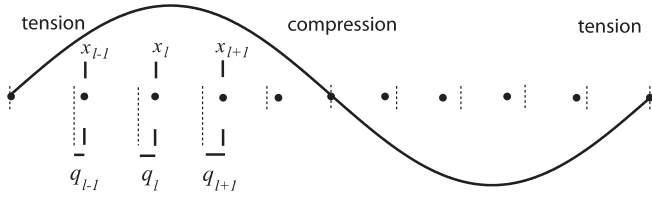


**Figure 1.** Representation of a one-dimensional solid in the presence of a longitudinal wave. Equilibrium positions of the atoms are given by the dashed lines, separated by a distance  $a$ , and actual positions are labeled by  $x_l$ . The sine wave is a representation of the displacement of the ions from equilibrium as a function of the horizontal position, with regions of tension and compression indicated. In the long wavelength approximation, the strain in the lattice is proportional to  $(q_{l+1} - q_l)$ . (Figure 3 is adapted from Reference 4).

where  $U(r, R_0)$  is the potential energy of the systems with the nuclei at fixed positions, and  $\Delta U(r, R)$  takes into account the change in potential energy of the system due to deviations of the nuclei from their equilibrium positions. To find the electron-phonon coupling within the Crude Adiabatic Approximation, we first write  $\Delta U(r, R)$  in a more useful form.

For the systems considered in this work, the wavefunctions of the optically active ion are highly localized to the central ion, and so we need concern ourselves mainly with the perturbation of the optically active ion by the motion of the surrounding ions. When the optically active ion is displaced from its equilibrium positions, the change in energy is due only to a *relative* change in the distance between the optically active ion and its neighbors. We denote the distance between the optically active ion and its neighbor (labeled  $\alpha$ ) as  $R_{ion,\alpha}$ , and the equilibrium distance between them as  $R_{ion,\alpha,0}$ . This change in potential energy between the ion and its neighbors, which we write as  $\Delta U_{ion}(r, R)$ , can be expressed in terms of a Taylor expansion:

$$\begin{aligned} \Delta U_{ion}(r, R) &= U_{ion}(r, R) - U_{ion}(r, R_0) \\ &= \sum_{\alpha} \left[ \frac{\partial U_{ion}}{\partial R_{\alpha}} \right]_{R_0} (R_{ion,\alpha} - R_{ion,\alpha,0}) + \frac{1}{2} \sum_{\alpha,\beta} \left[ \frac{\partial^2 U_{ion}}{\partial R_{ion,\beta} \partial R_{ion,\alpha}} \right]_{R_0} \\ &\quad \times (R_{ion,\alpha} - R_{ion,\alpha,0}) (R_{ion,\alpha} - R_{ion,\beta,0}) + \dots \\ &= \Delta U_{ion}^{(1)} + \Delta U_{ion}^{(2)} + \dots \end{aligned} \quad [4]$$

where  $\Delta U_{ion}^{(1)}$  and  $\Delta U_{ion}^{(2)}$  are given by

$$\Delta U_{ion}^{(1)} = \sum_{\alpha} \left[ \frac{\partial U_{ion}}{\partial R_{\alpha}} \right]_{R_0} (R_{ion,\alpha} - R_{ion,\alpha,0}) \quad [5]$$

$$\Delta U_{ion}^{(2)} = \frac{1}{2} \sum_{\alpha,\beta} \left[ \frac{\partial^2 U_{ion}}{\partial R_{ion,\beta} \partial R_{ion,\alpha}} \right]_{R_0} (R_{ion,\alpha} - R_{ion,\alpha,0}) (R_{ion,\alpha} - R_{ion,\beta,0}) \quad [6]$$

In order to gain some physical insights into these terms, consider the simple case of a linear solid, shown in Figure 1. The atoms are separated from their neighbors by a distance  $a$ , and are free to vibrate longitudinally. The displacement of the  $l^{\text{th}}$  ion from its equilibrium position is given by  $q_l$ . In addition to the displacements, Figure 1 also shows a representation of the longitudinal acoustic wave in the crystal. In the long wavelength approximation, the strain,  $\epsilon_l$ , at the  $l^{\text{th}}$  site can be written as:<sup>4</sup>

$$\epsilon_l = \frac{\partial q_l}{\partial x} \approx \frac{q_{l+1} - q_l}{a} = \frac{(x_{l+1} - x_l) - a}{a} \quad [7]$$

Thus, the strain is proportional to the change in distance between the optically active ion and a neighboring ion. In the case of an ion in a solid,  $(x_{l+1} - x_l) - a$  in 7 is replaced by  $R_{ion,\alpha} - R_{ion,\alpha,0}$ . Comparing 7 and 4, the change in potential energy experienced by the optically active ion due to the displacements of the ions in the solid can be

written as the sum of powers of the strain.

$$\Delta U_{ion}(r, R) = \sum_{\alpha} V_{1,\alpha} \epsilon_{\alpha} + \sum_{\alpha} V_{2,\alpha} \epsilon_{\alpha}^2 + \dots \quad [8]$$

For a linear system of like ions experiencing a longitudinal wave, as shown in Figure 3, the form of the strain given in 7 is particularly simple. For a three dimensional crystal consisting of different ion types, transverse and longitudinal waves, and going beyond the long wavelength limit, the situation is much more complex. We shall, however, make the assumption that we can write the  $\Delta U_{ion}(r, R)$  in the form given in 8.

Threating  $\Delta U_{ion}^{(1)}$  as a perturbation, the electronic wavefunction corrected to the first order is:

$$\phi_i^{(1)}(r, R) = \phi_i^0(r, R_0) + \sum_{j \neq i} \frac{\langle \phi_j^0(r, R_0) | \Delta U_{ion}^{(1)} | \phi_i^0(r, R_0) \rangle}{\epsilon_j - \epsilon_i} \phi_j^0(r, R_0) \quad [9]$$

Thus, the first order corrected states in the Crude Adiabatic Approximation are:

$$\begin{aligned} \Psi_{i,k}^{(1)}(r, R) &= \left[ \phi_i^0(r, R_0) + \sum_{j \neq i} \frac{\langle \phi_j^0(r, R_0) | \Delta U_{ion}^{(1)} | \phi_i^0(r, R_0) \rangle}{\epsilon_j - \epsilon_i} \phi_j^0(r, R_0) \right] \chi_k(R) \end{aligned} \quad [10]$$

The sum in 10 contains terms of the form  $\langle \phi_j^0(r, R_0) | \Delta U_{ion}^{(1)} | \phi_i^0(r, R_0) \rangle$ , which mix the various electronic states of the system, indicating that the displacements of the nuclei from equilibrium cause transitions from one electronic state to another. Thus,  $\Delta U_{ion}^{(1)}$  is an example of an electron-phonon coupling operator. It is interesting to note that the wavefunctions in 10 are the product of a purely electronic wavefunction, in brackets  $[\ ]$ , with nuclear wavefunction. That is, when  $\Delta U_{ion}^{(1)}$  is used as a perturbation to the electronic wavefunction only, it mixes various electronic states, but does not couple the electronic wavefunction to the vibrational wavefunction. The electronic and the nuclear states are not truly coupled in the usual sense, and the corrected wavefunction 10 is still considered “adiabatic”. This type of the coupling is known as *electron-phonon coupling of type A*.<sup>6</sup>

*Type B electron-phonon coupling.*— In the Born Oppenheimer Adiabatic Approximation, the states of the system are given by 1. In arriving at Equation 1 as a solution to the Schrödinger Equation for an ion in a solid, certain terms in the full Hamiltonian were ignored. As shown any of References 1–9, these terms originate from the terms in the full Hamiltonian associated with the kinetic energy of the nuclei. Specifically, operating on the Born-Oppenheimer wavefunction (Equation 1) with the nuclear kinetic energy operator gives

$$\begin{aligned} -\frac{\hbar^2}{2M_{\alpha}} \bar{\nabla}_{\alpha}^2 \phi(r, R) \chi(R) &= -\frac{\hbar^2}{2M_{\alpha}} \bar{\nabla}_{\alpha} \cdot \left[ \bar{\nabla}_{\alpha} (\phi \chi) \right] \\ &= -\frac{\hbar^2}{2M_{\alpha}} \bar{\nabla}_{\alpha} \cdot \left( \phi \bar{\nabla}_{\alpha} \chi + \chi \bar{\nabla}_{\alpha} \phi \right) \\ &= -\frac{\hbar^2}{2M_{\alpha}} \left\{ \phi \bar{\nabla}_{\alpha}^2 \chi + \chi \bar{\nabla}_{\alpha}^2 \phi + 2 \left( \bar{\nabla}_{\alpha} \phi \right) \cdot \left( \bar{\nabla}_{\alpha} \chi \right) \right\} \end{aligned} \quad [11]$$

Because the last two terms in brackets  $\{ \}$  on the right of Equation 11 contain derivatives of the electronic wavefunction with respect to the nuclear coordinates, they couple the nuclear motion to the electronic motion. We define a non-adiabatic Hamiltonian,  $H_{NA}$ , by the last two

terms in 11 in the following manner.

$$H_{NA}\Psi_{i,k}(r, R) = -\frac{\hbar^2}{2} \sum_{\alpha} \frac{1}{M_{\alpha}} \chi_{i,k}(R) \vec{\nabla}_{\alpha}^2 \phi_i(r, R) - \hbar^2 \sum_{\alpha} \frac{1}{M_{\alpha}} (\vec{\nabla}_{\alpha} \phi_i(r, R)) \cdot (\vec{\nabla}_{\alpha} \chi_{i,k}(R)) \quad [12]$$

At this point, it is typical to assume that the first term on the right in 12 is negligible compared with the second. Under that assumption, 12 becomes

$$H'_{NA}\Psi_{i,k}(r, R) = -\hbar^2 \sum_{\alpha} \frac{1}{M_{\alpha}} (\vec{\nabla}_{\alpha} \phi_i(r, R)) \cdot (\vec{\nabla}_{\alpha} \chi_{i,k}). \quad [13]$$

Treating  $H'_{NA}$  as a perturbation, the first order, non-adiabatic wavefunction is given by:

$$\Psi_{i,k}^{(1)}(r, R) = \Psi_{i,k}(r, R) - \sum_{j \neq i} \sum_{\alpha} \frac{\hbar^2}{M_{\alpha}} \frac{(\Psi_{j,k}(r, R)) (\vec{\nabla}_{\alpha} \phi_i(r, R)) \cdot (\vec{\nabla}_{\alpha} \chi_{i,k})}{E_j - E_i} |\Psi_{i,k}(r, R)\rangle \times \Psi_{j,k}(r, R) \quad [14]$$

The wavefunction  $\Psi_k^{(1)}$  in 14 cannot be expressed as a product of an electronic wavefunction and a nuclear wavefunction, so it is a true non-adiabatic wavefunction.  $H'_{NA}$  is referred to as the *electron-phonon coupling of type B*.<sup>6</sup>

### Representation of Eigenstates and Operators

In order to apply the previous treatments to phonon-related processes in solids, we must first represent the vibrational states of the lattice and electron-phonon coupling operators in the appropriate forms. To do so, we make the following assumptions:

1. *The nuclei vibrate in a harmonic potential.* In this so-called ‘‘harmonic approximation’’, each normal coordinates  $Q_k$ , is associated with the  $k^{\text{th}}$  vibrational mode of the solid and oscillates with a frequency  $\omega_k$ . Each mode acts as a harmonic oscillator, with the excitation of the  $k^{\text{th}}$  oscillator corresponding to the number of phonons,  $n_k$ , in that mode. The energy of the lattice is:

$$E = E_0 + \sum_k \left( n_k + \frac{1}{2} \right) \hbar \omega_k \quad [15]$$

where  $E_0$  is the energy of the lattice with the nuclei at their equilibrium positions.

2. *The normal modes of the solid act independently, with no communication between them.* In this assumption, the eigenstates of the lattice vibrations,  $\chi(Q_k)$ , are products of the states of the normal modes:

$$\chi(Q_k) = \prod_k |n_k\rangle = |n_1\rangle |n_2\rangle |n_3\rangle \dots |n_k\rangle \dots |n_{3N-6}\rangle, \quad [16]$$

where  $N$  is the number of atoms in the solid.

It should be noted that neither of the assumptions above are strictly valid. Experiments on phonon decay times have shown that phonons generally do decay into other, lower energy modes [e.g. 10, 11]. Also, the assumption of a harmonic approximation is only valid for very small amplitudes of vibration. As the amplitudes increase (i.e., as temperature increases), the restoring force becomes increasingly non-linear. Frenkel noted early on that such non-linear effects cause a breakdown of the adiabatic separation between the electronic and nuclear subsystems, thus allowing lattice vibrations to cause electronic transitions.<sup>12</sup> Despite these assumptions, working with the states as described in 16 does lead to results that adequately explain the behavior of many systems across a range of temperatures.

In order to make use of 16, the electron-phonon coupling operators must be expressed in terms of the normal coordinates of the lattice. For the electron-phonon coupling of type A, given in terms of the strain operator in Equation 8, it is convenient to express the strain in terms of the phonon annihilation and creation operators,  $a$  and  $a^{\dagger}$ , respectively. We do not derive this expression here, but simply present the result. The reader is referred to the text by Henderson and Imbusch<sup>4</sup> for details of the derivation.

Referring to the case of a linear solid shown in Figure 1, it can be shown that the displacement of the  $l^{\text{th}}$  ion from its equilibrium position,  $q_l$ , can be written in terms of the generalized position has the following form:<sup>4</sup>

$$q_l = \left( \frac{1}{N} \right)^{1/2} \sum_k Q_k \exp(-i\kappa a) \quad [17]$$

where  $a$  is the spacing between atoms,  $\kappa$  is the wave vector associated with the  $k^{\text{th}}$  mode,  $N$  is the number of atoms in the linear chain. Using 17, the local strain at the site of the  $l^{\text{th}}$  ion, as approximated in 8, due to the  $k^{\text{th}}$  normal mode can be expressed in terms of  $a_k$  and  $a_k^{\dagger}$  as follows:

$$\varepsilon_k = -i \left( \frac{\hbar \omega_k}{2MNv_k^2} \right)^{1/2} (a_k^{\dagger} - a_k), \quad [18]$$

where  $v_k$  is the velocity of the sound associated with the  $k^{\text{th}}$  mode. Again, the reader is referred to Ref. 4 for the full derivation of 18. The operator for the electron-phonon coupling of type A is obtained by inserting 18 into the expansion similar to 8, except the sum is over all the normal coordinates. Keeping only the first two terms, the result is:

$$\Delta U_{ion} \approx \Delta U_{ion}^{(1)} + \Delta U_{ion}^{(2)} = V_{1,k} \varepsilon_k + V_{2,k} \varepsilon_k^2 \quad [19]$$

Recall that 19 applies to a linear chain of atoms in the long wavelength approximation. For practical reasons, however, it is usually assumed that the simplified version of the strain operator in 18 has the same form for all normal modes in a three-dimensional crystal.

The electron phonon coupling of type B is given by the non-adiabatic Hamiltonian,  $H'_{NA}$ , defined by Equation 13. To express 13 in terms of the normal coordinates, recall that  $i\hbar \vec{\nabla}_{\alpha} = \vec{P}_{\alpha}$ . The kinetic energy of the lattice in Cartesian coordinates and in normal coordinates is:

$$T_N = \sum_{\alpha} \frac{\vec{P}_{\alpha}^2}{2M_{\alpha}} = \sum_k \frac{\vec{P}_k^2}{2M_k} = -\frac{\hbar^2}{2} \sum_k \frac{1}{M_k} \left( \frac{\partial}{\partial Q_k} \right)^2 \quad [20]$$

where the first sum is over all nuclei, the second and third sums are over all normal modes, and the  $M_k$  are properly weighted masses. Using the term on the far right in 20, and re-deriving Equation 13, it is readily seen that the electron-phonon coupling operator of type B operating on the adiabatic wavefunction of the system is expressed as:

$$H'_{NA}\Psi_i(r, Q) = -\hbar^2 \sum_k \frac{1}{M_k} \left( \frac{\partial \phi_i(r, Q)}{\partial Q_k} \right) \cdot \left( \frac{\partial \chi_i(Q)}{\partial Q_k} \right) \quad [21]$$

This is the operator representing the electron-phonon coupling of type B written in terms of the normal coordinates of the lattice. We note that calculating the first term in parentheses in 21 is very difficult, requiring detailed knowledge of the electronic wavefunction. On the other hand, the last term in the sum in 21 is readily calculated in the harmonic approximation, since it contains the first derivatives of the standard harmonic oscillator wavefunctions. The matrix elements containing this term are frequently calculated in determining non-radiative transition rates between electronic levels using a single configurational coordinate model [13, 14 and references therein].

### Thermal Broadening and Shifting of Sharp Spectral Lines

*Thermal broadening of spectral lines.*— The broadening of a spectral line can be caused by several interactions, among which are the following:

$$\begin{aligned}
 \langle \Psi_f | \Delta U_{ion} | \Psi_i \rangle &= \sum_j \frac{\langle \phi_i^0, n_k - 1, n_{k'} + 1 | \Delta U_{ion}^{(1)} | \phi_j^0, n_k - 1, n_{k'} \rangle \langle \phi_j^0, n_k - 1, n_{k'} | \Delta U_{ion}^{(1)} | \phi_i^0, n_k, n_{k'} \rangle}{\epsilon_i - (\epsilon_j - \hbar\omega_k)} \\
 &+ \sum_j \frac{\langle \phi_i^0, n_k - 1, n_{k'} + 1 | \Delta U_{ion}^{(1)} | \phi_j^0, n_k - 1, n_{k'} \rangle \langle \phi_j^0, n_k, n_{k'} + 1 | \Delta U_{ion}^{(1)} | \phi_i^0, n_k, n_{k'} \rangle}{\epsilon_i - (\epsilon_j - \hbar\omega_{k'})} \\
 &+ \langle \phi_i^0, n_k - 1, n_{k'} + 1 | \Delta U_{ion}^{(2)} | \phi_i^0, n_k, n_{k'} \rangle. \quad [24]
 \end{aligned}$$

1. Strain Broadening - These are site-to-site variations in the crystalline field at the ion due to strains in the crystal. This is a static interaction and is present at even low temperatures.
2. Lifetime Broadening: This category includes all processes that affect the lifetime ( $\tau$ ) of the ion in its excited state, thereby changing the linewidth ( $\Delta E$ ) through the uncertainty relation:  $\Delta E\tau \geq \hbar/2$ . The processes are radiative decay, nonradiative decay, and vibronic transitions. Even for allowed transitions, the broadening due to this term is less than the strain broadening observed in single crystals.
3. Direct processes: These processes involve a transition from one level to another via the absorption or emission of a phonon. This term has been found to be of secondary importance in most systems, and so will not be discussed here.
4. Raman Scattering: This occurs via the emission of a phonon from one mode and the absorption of a phonon from a different mode. The initial and final electronic states are the same, and the intermediate electronic state is virtual. It is a second order process, and is found to be the dominant contributor to the line broadening in several systems [e.g. 15-18]. This process is shown in Figure 2.

To investigate this interaction, we utilize the electron-phonon coupling of type A, as given by Equations 18 and 19. Note that this form of the adiabatic approximation utilized the Crude Adiabatic Approximation, and so is only valid for systems for which the relevant electronic states have nearly the same equilibrium position. For more strongly coupled systems, we refer readers to, for example, References 4 and 19.

For weak electron-phonon coupling, Equations 18 and 19 can be used to determine the interaction term to the second order. The result is:

$$\begin{aligned}
 \Delta U_{ion} &\approx \Delta U_{ion}^{(1)} + \Delta U_{ion}^{(2)} \\
 &= V_1 \sum_k \left( \frac{\hbar\omega_k}{2Mv^2} \right)^{1/2} (\mathbf{a}_k - \mathbf{a}_k^\dagger) \\
 &+ V_2 \frac{\hbar}{2Mv^2} \sum_k \sqrt{\omega_k\omega_{k'}} (\mathbf{a}_k - \mathbf{a}_k^\dagger)(\mathbf{a}_{k'} - \mathbf{a}_{k'}^\dagger) \quad [22]
 \end{aligned}$$

where we have assumed  $V_1$  and  $V_2$  are independent of the phonon mode  $k$ . The states of the system are products of an electronic part and a nuclear part.

$$|\Psi\rangle = |\phi\rangle \otimes |n_1 n_2 n_3 \dots n_k \dots\rangle = |\phi, n_1 n_2 n_3 \dots n_k \dots\rangle \quad [23]$$

Since Raman scattering is a second order process, the contributing terms derive from

1. the first order term in 22 with the first order correction to the initial and final states, and
2. the second order term in 22 with the zero<sup>th</sup> order states.

The relevant matrix element for the Raman process is:

Using 22 to replace for  $\Delta U_{ion}^{(1)}$  and  $\Delta U_{ion}^{(2)}$  in 24, recalling that  $\mathbf{a}|n\rangle = \sqrt{n}|n-1\rangle$  and  $\mathbf{a}^\dagger|n\rangle = \sqrt{n+1}|n+1\rangle$ , and assuming that  $\hbar\omega_k, \hbar\omega_{k'} \ll \epsilon_j$  for all intermediate electronic states,  $j$ , 24 becomes:

$$\langle \Psi_f | \Delta U_{ion} | \Psi_i \rangle = \alpha' \sqrt{\omega_k \omega_{k'} n_k (n_{k'} + 1)} \quad [25]$$

where

$$\alpha' = \frac{\hbar}{Mv^2} \left[ \sum_{j \neq i} \frac{|\langle \phi_j^0 | V_1 | \phi_i^0 \rangle|^2}{\epsilon_i - \epsilon_j} + \langle \phi_i^0 | V_2 | \phi_i^0 \rangle \right]. \quad [26]$$

The transition probability per unit time due to modes  $k$  and  $k'$  is

$$(W_{Raman})_{kk'} = \frac{2\pi}{\hbar^2} |\alpha'|^2 \omega_k \omega_{k'} n_k (n_{k'} + 1) \varrho(\omega_f), \quad [27]$$

where  $\varrho(\omega_f)$  represents the density of final states of the phonon field. To find the total transition rate for these Raman processes, we must integrate over all phonon modes  $k$  and  $k'$ . For sharp lines, where the width of the line is much less than the Debye frequency, we estimate  $\varrho(\omega_f)$  as

$$\varrho(\omega_f) \simeq \varrho(\omega_k) \varrho(\omega_{k'}) \delta(\omega_k - \omega_{k'}) d\omega_k d\omega_{k'} = \varrho^2(\omega_k) d\omega_k. \quad [28]$$

Inserting 28 into 27 and integrating over all phonon modes, we obtain:

$$W_{Raman} = \frac{2\pi}{\hbar^2} |\alpha'|^2 \int \omega^2 n(n+1) \varrho^2(\omega) d\omega \quad [29]$$

Recalling the expression for the phonon occupation number of the  $k^{\text{th}}$  mode,

$$n = \frac{1}{e^{\hbar\omega/kT} - 1}, \quad [30]$$

the total transition probability becomes

$$W_{Raman} = \frac{2\pi}{\hbar^2} |\alpha'|^2 \int \omega^2 \varrho^2(\omega) \frac{e^{\hbar\omega/kT}}{(e^{\hbar\omega/kT} - 1)^2} d\omega. \quad [31]$$

In the Debye approximation,  $\varrho(\omega) = 3V\omega^2/2\pi^2 v_s^3$ , 31 takes the following form:

$$W_{Raman} = \frac{2\pi}{\hbar^2} |\alpha'|^2 \frac{9V^2}{4\pi^4 v_s^6} \int_0^{\omega_D} \frac{\omega^6 e^{\hbar\omega/kT}}{(e^{\hbar\omega/kT} - 1)^2} d\omega, \quad [32]$$

where  $\omega_D$  is the Debye frequency. It is convenient to rewrite 32 in terms of the unitless parameter  $x = \hbar\omega/kT$  and the Debye temperature  $T_D = \hbar\omega_D$ . The result is:

$$W_{Raman} = \bar{\alpha} \left( \frac{T}{T_D} \right)^7 \int_0^{T_D/T} \frac{x^6 e^x}{(e^x - 1)^2} dx. \quad [33]$$

where  $\bar{\alpha} = \frac{9V^2}{2\pi\hbar^2} \left( \frac{\omega_D}{v_s} \right)^6 |\alpha'|^2$ , and is referred to as the electron-phonon coupling constant. The temperature dependence of 33 is contained in the  $T^7$  term outside the integral and in the upper limit of the integral,  $T_D/T$ . In the limit as  $T \rightarrow 0$ , the upper limit goes to infinity, and the integral is simply a constant. Thus, the contribution of Raman processes to

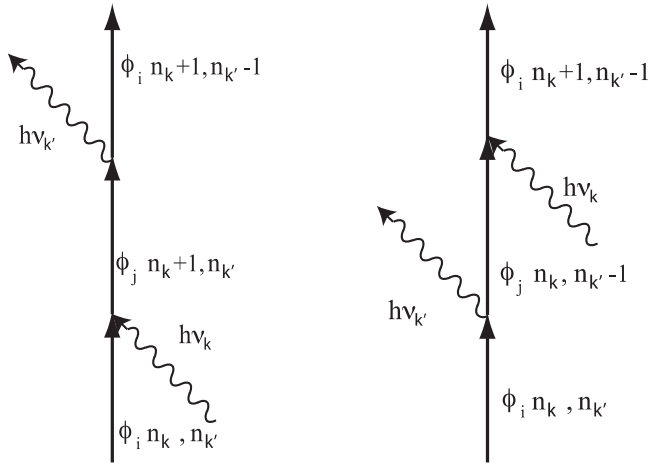


**Figure 2.** The Raman process: Both diagrams above show the absorption of a phonon of frequency  $\nu_k$  then the emission of a phonon of (frequency  $\nu_{k'}$ ). The initial, intermediate and final states are indicated.

the linewidth goes as  $T^7$ , which goes to zero as  $T \rightarrow 0$ , as expected. At high temperatures ( $T \gg T_D$ ) we may use the approximation  $e^x \sim 1 + x$ , so the integral goes roughly as  $x^5$ , and the temperature dependence goes as  $T^2$ .

In many systems, the contribution of the Raman term at low temperatures is much less than the residual linewidth, which is due to inhomogeneous broadening by variations in the sites of the ions in the lattice. In such systems, the linewidth is given by an equation of the form [e.g. 15–17],

$$\Delta\epsilon = \Delta\epsilon_0 + \bar{A} \frac{1}{x^7} \int_0^x \frac{x^6 e^x}{(e^x - 1)^2} dx, \quad [34]$$

where  $\Delta\epsilon_0$  represents the residual linewidth and  $A$  is proportional to the electron-phonon coupling constant. A graph of the function described in 34 is shown in Figure 3 for various values of  $\Delta\epsilon_0$ . The units used are arbitrary, and the graph is simply intended to show the temperature dependence of the thermal contribution to the linewidth. As seen in Figure 3, at high temperatures the slope of the line approaches  $-2$ , corresponding to a  $T^2$  dependence. Note that the slope is allowed to have a  $T^n$  dependence where  $n$  is greater than 2, especially when the residual linewidth is small.

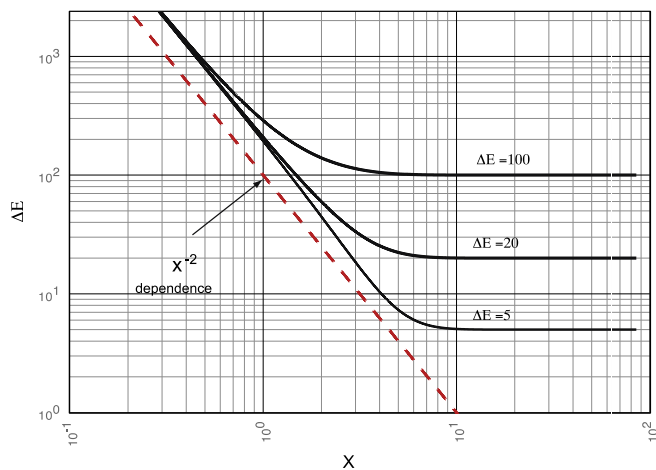


**Figure 3.** Plot (solid lines) of Equation 34 vs.  $x$  relevant to the thermal broadening of a spectral line for systems with three different values of the residual linewidths. The variable  $x$  is related to temperature by  $x = \hbar\omega/kT$ , so temperature increases to the left. Values of the residual linewidths, in arbitrary units, are also shown. The dotted line shows a  $T^2$  dependence.

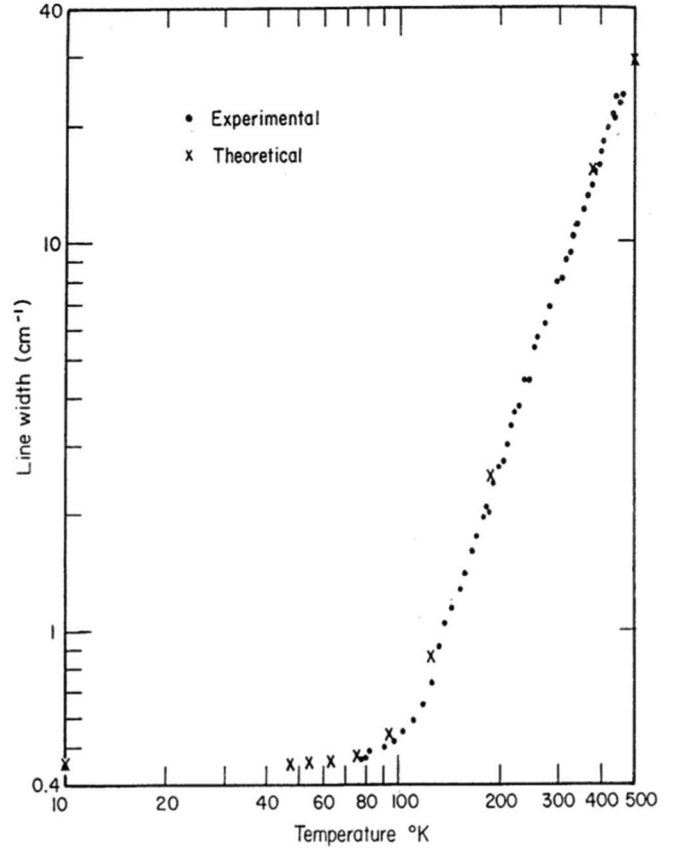


**Figure 4.** Log-log plot of the temperature dependence of the linewidth of the  ${}^2E \rightarrow {}^4A_2$  transition of  $V^{4+}$  in bulk MgO. The residual linewidth is on the order of  $0.45 \text{ cm}^{-1}$ , and the slope of a best fit line to the data at high temperatures is  $\sim 2.2$ .<sup>16</sup>

Experimental results of linewidths of sharp lines in solids are consistent with Equation 34.<sup>15–17</sup> One example of this is the thermal dependence of the linewidth of the  ${}^2E \rightarrow {}^4A_2$  transition of  $V^{4+}$  in MgO between 4 K and 460 K, as shown in Figure 4.<sup>16</sup> The residual linewidth of  $\sim 0.45 \text{ cm}^{-1}$  is observed at low  $T$ , and a near constant slope of  $\sim 2$  at  $T > 150 \text{ K}$ . In that work, the best fit line to Equation 33 was found for  $T_D = 760 \text{ K}$  and  $\bar{\alpha} = 377 \text{ cm}^{-1}$ .

*Thermal shifting of spectral lines.*— Any interaction of a system an external agent will, in general, affect the energies of the states of the system. Thus, we expect that phonons interacting with an ion in a solid will shift the energy levels of the ion. As temperature increases, these interactions also increase, leading to the so-called thermal shift of the energy level. In a perturbation treatment, the change in energy the level found in the diagonal matrix elements containing the Hamiltonian of the perturbing interaction, i.e., matrix elements for which the initial and final states of the system are unchanged. The contribution of the electron-phonon interaction is a second-order effect, and so contains the matrix element of  $\Delta U_{ion}^{(2)}$  between the zero<sup>th</sup> order states, and of  $\Delta U_{ion}^{(1)}$  between the first order states. The relevant Raman processes involve the virtual absorption and emission of phonon of the same frequency. The correction to the energy of the electronic state due to the electron-phonon interaction is given by:

$$\begin{aligned} \Delta\epsilon_{i,k} = & \langle \phi_i, n_k | \Delta U_{ion}^{(2)} | \phi_i, n_k \rangle \\ & + \sum_j \frac{\langle \phi_i, n_k | \Delta U_{ion}^{(1)} | \phi_j, n_k - 1 \rangle \langle \phi_j, n_k - 1 | \Delta U_{ion}^{(1)} | \phi_i, n_k \rangle}{\epsilon_i - (\epsilon_j - \hbar\omega_k)} \\ & + \sum_j \frac{\langle \phi_i, n_k | \Delta U_{ion}^{(1)} | \phi_j, n_k + 1 \rangle \langle \phi_j, n_k + 1 | \Delta U_{ion}^{(1)} | \phi_i, n_k \rangle}{\epsilon_i - (\epsilon_j + \hbar\omega_k)} \end{aligned} \quad [35]$$

Using 49 and 50 to rewrite  $\Delta U_{ion}^{(1)}$  and  $\Delta U_{ion}^{(2)}$  in terms of the creation and annihilation operators, and assuming that  $|\epsilon_i - \epsilon_j| \gg \hbar\omega_k$ , 35 becomes

$$\begin{aligned} \Delta\epsilon_{i,k} = & \frac{\hbar\omega}{Mv_s^2} \langle \phi_i | V_2 | \phi_i \rangle \langle n_k | (a_k^\dagger a_k + a_k a_k^\dagger) | n_k \rangle \\ & + \frac{\hbar\omega_k}{Mv_s^2} \sum_j \frac{|\langle \phi_j | V_1 | \phi_j \rangle|^2}{\epsilon_i - \epsilon_j} \\ & \times \left\{ \begin{aligned} & \langle n_k | (a_k - a_k^\dagger) | n_k - 1 \rangle \langle n_k - 1 | (a_k - a_k^\dagger) | n_k \rangle \\ & + \langle n_k | (a_k - a_k^\dagger) | n_k + 1 \rangle \langle n_k + 1 | (a_k - a_k^\dagger) | n_k \rangle \end{aligned} \right\} \end{aligned} \quad [36]$$

Using the identities  $a|n\rangle = \sqrt{n}|n-1\rangle$  and  $a^\dagger|n\rangle = \sqrt{n+1}|n+1\rangle$ , 36 reduces to

$$\Delta\epsilon_{i,k} = \frac{\hbar}{Mv_s^2} \left[ \langle \phi_i | V_2 | \phi_i \rangle + \sum_j \frac{|\langle \phi_j | V_1 | \phi_j \rangle|^2}{\epsilon_i - \epsilon_j} \right] \omega_k (2n_k + 1) \quad [37]$$

The thermal shift of the line is due only to the terms containing  $n_k$ . The total thermal shift is found by summing over all  $k$ . For *large particles*, this sum can be approximated by an integral, so the total shift is given by:

$$\Delta\epsilon_i = \frac{\hbar}{Mv_s^2} \left[ \langle \phi_i | V_2 | \phi_i \rangle + \sum_j \frac{|\langle \phi_j | V_1 | \phi_j \rangle|^2}{\epsilon_i - \epsilon_j} \right] 2 \int \rho(\omega_k) \omega_k n_k d\omega_k \quad [38]$$

Assuming the Debye distribution ( $\rho(\omega) = 3V\omega^2/2\pi^2v_s^3$ ), using the equilibrium value of  $n_k$  as defined in 30, setting the upper limit of the integral in 38 to the Debye frequency, and making the substitution  $x = \hbar\omega/kT$ , the thermal shift of an energy level becomes:

$$\delta E_{ther} = \Delta V \int_0^{T_D/T} \frac{x^3}{e^x - 1} dx \quad [39]$$

where

$$\Delta V = \frac{2\hbar}{Mv_s^2} \left( \frac{kT}{\hbar} \right)^4 \left[ \langle \phi_i | V_2 | \phi_i \rangle + \sum_j \frac{|\langle \phi_j | V_1 | \phi_j \rangle|^2}{\epsilon_i - \epsilon_j} \right] \quad [40]$$

Experimental measurements of lineshifts involve transitions between two levels, so the measured lineshift is the difference between the shifts of the initial and final energy levels of the transition. It is generally assumed that the measured shift will follow the same temperature dependence as in 39, though  $\Delta V$  will be different than in 40. Thus, the experimentally measured thermal shift of a spectral line will be described by the following:

$$\delta E_{ther} = \Delta V' \int_0^{T_D/T} \frac{x^3}{e^x - 1} dx \quad [41]$$

The temperature dependence of the thermal shift of a spectral line is determined by the  $T^4$  term contained in  $\Delta V'$  and by the upper limit of the integral. As  $T \rightarrow 0$ , the integral approaches a constant value, and the line shift goes as  $T^4$ . For large  $T$ , the integrand goes roughly as  $x^2$ , the integral goes as  $T^{-3}$ , and so the line shift is linear with  $T$ .

An example of this lineshift can also be found in the work by Di Bartolo et al.,<sup>16</sup> who measured the shift of the  ${}^2E \rightarrow {}^4A_2$  transition of  $V^{4+}$  in MgO between 77 and 450 K, shown in Figure 5. The data in Figure 5 show a decreasing slope as temperature increases, changing from  $T^3$  at low temperatures to  $\sim T^{1.5}$  at higher temperatures, which is consistent with Equation 41.

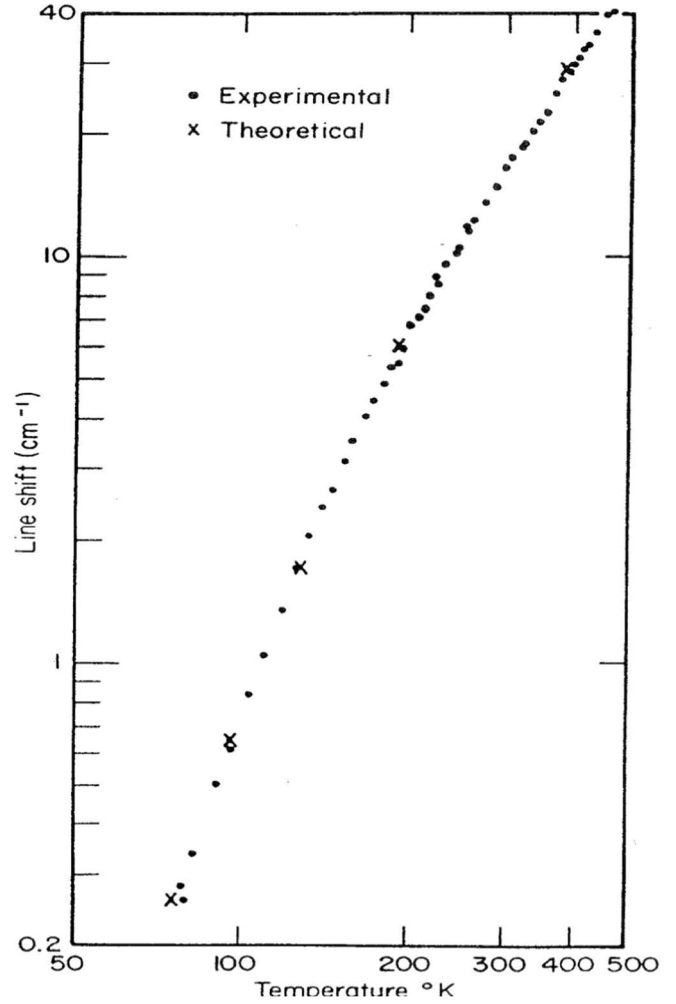


**Figure 5.** Log-log plot of the temperature dependence of the line shift of the  ${}^2E \rightarrow {}^4A_2$  transition of  $V^{4+}$  in bulk MgO.<sup>16</sup> The temperature dependence is  $\sim T^{3.5}$  and low temperature and  $T^{1.2}$  at high temperature, consistent with Equation 39.

### The Phonon Density of States in Nanoparticles

To examine the phonon density of states (DOS) of a nanoparticle, we consider a cubic solid with side length  $L$  and atomic spacing  $a$ . The allowed standing waves in the crystal have wavelengths  $2L/n$ , where  $n = (n_x^2 + n_y^2 + n_z^2)^{1/2}$ , and  $n_x, n_y, n_z$  are integers ranging from 1 to  $L/a$ . These wavelengths correspond to resonances in the crystal and determine its phonon modes. The energy of a phonon in such a solid is given by

$$\epsilon_{ph} = \frac{\hbar v_s}{\lambda} = \frac{\hbar v_s}{2L} n, \quad [42]$$

where  $v_s$  is the velocity of sound in the crystal. Note that the maximum phonon energy (when  $n = \sqrt{3}L/a$ ) is determined by the interatomic spacing, and so is independent of the particle size, while the low frequency phonons increase in energy as particle size decreases. Consequently, many low frequency phonon modes that exist in the bulk are no longer supported in a nanoparticle.

The phonon DOS of cubic nanoparticles  $15 \times 15 \times 15$  atoms ( $L \sim 3$  nm),  $25 \times 25 \times 25$  atoms ( $L \sim 5$  nm), and  $250 \times 250 \times 250$  atoms ( $L \sim 50$  nm) have been calculated using the speed of sound equal to 3400 m/s and an interatomic spacing of 0.2 nm. The modes were accumulated in 1000 bins, each approximately  $0.5 \text{ cm}^{-1}$  in width. The results are shown in Figure 6. We note the following:

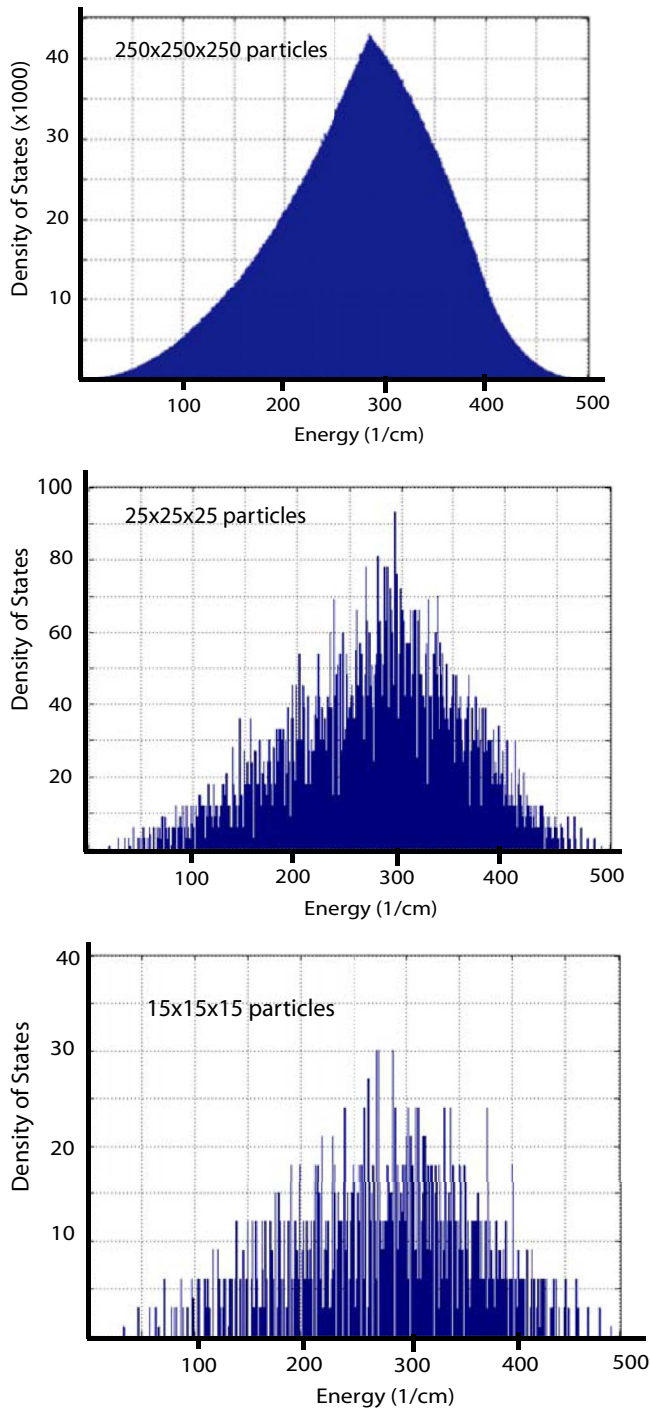


**Figure 6.** The phonon density of states vs. phonon energy of cubic nanoparticles with  $250 \times 250 \times 250$  atoms,  $25 \times 25 \times 25$  atoms, and  $15 \times 15 \times 15$  atoms. The velocity of sound was set to 3400 m/s.

1. For the  $250 \times 250 \times 250$  atoms system, the phonon DOS exhibits an  $\varepsilon^2$  dependence, as expected from the Debye theory, out to a frequency at which the DOS reaches a maximum. At higher energies, the phonon DOS is decidedly un-Debye-like, decreasing smoothly to zero. This behavior is due to the finite size of the crystal, as well as its cubic shape.
2. For the smaller particles, the phonon DOS as a discrete function, especially at lower energies, with a large energy gap between zero energy and the first mode. For 50 nm particle, however, the DOS appears nearly continuous at all energies, and is similar in

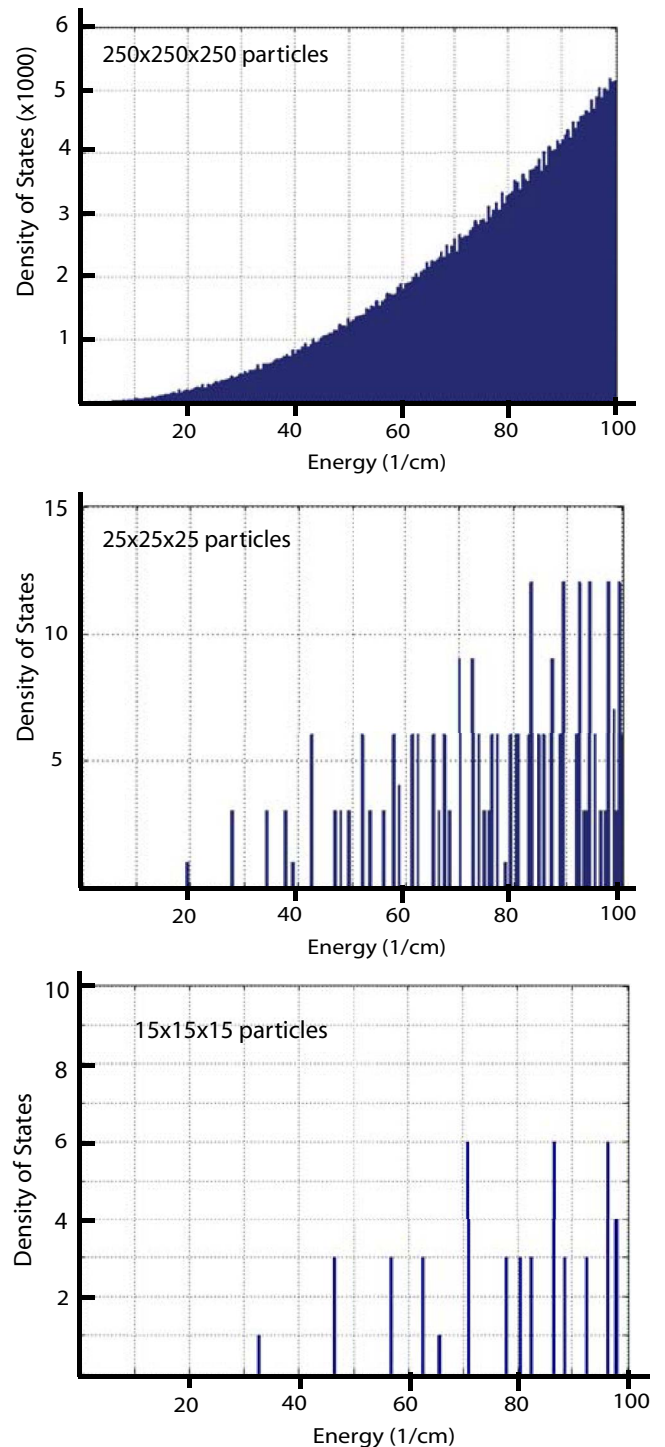


**Figure 7.** The phonon density of states at low phonon energies of cubic nanoparticles with  $250 \times 250 \times 250$  atoms,  $25 \times 25 \times 25$  atoms, and  $15 \times 15 \times 15$  atoms. The velocity of sound was set to 3400 m/s.

3. The results in Figures 6 and 7 are for cubic crystals, but the discreteness of the DOS at low energies is a common feature to all very small particles.

The discreteness of the phonon DOS of a small particle is due to the fact that in going from a bulk crystal to a nanoparticle, the

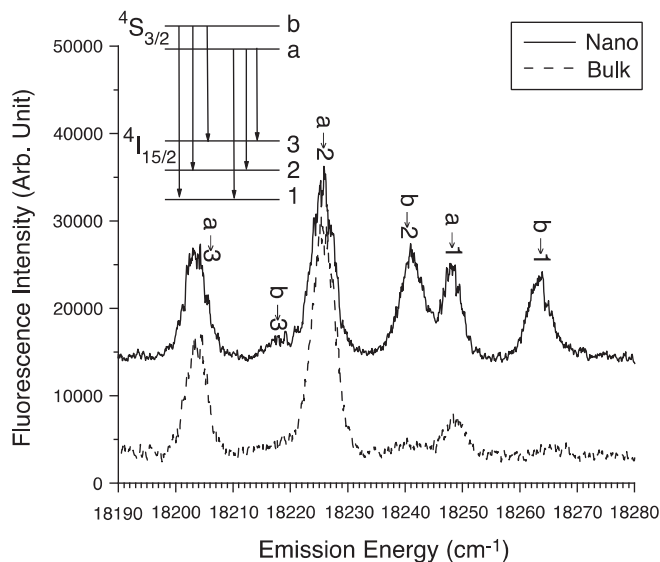


**Figure 8.** Emission spectra of the  $^4S_{3/2}$  to  $^4I_{15/2}$  transition in bulk (dotted line) and nanocrystals (solid line) of Er:Y<sub>2</sub>O<sub>2</sub>S at 2.6 K.<sup>20</sup>

total number of phonon modes decreases drastically. This decrease is easily estimated by noting that the total number of phonon modes is simply  $3N-6$ , where  $N$  is the number of atoms in the particle.  $N$  can be estimated as

$$N \sim \left(\frac{L}{a}\right)^3 \quad [43]$$

For a bulk crystal with  $L = 0.3$  cm and  $a = 0.2$  nm,  $3N \sim 4.5 \times 10^{21}$ , whereas when  $L = 3$  nm,  $3N \sim 4.5 \times 10^3$ . Thus, going from a particle size of 0.3 cm to 3 nm the total number of allowed phonon modes decreases by 18 orders of magnitude! As a result, the phonon spectrum is no longer a continuous function of energy.

Given the importance that phonon-related processes play in the luminescence from ions in solids, the change in the phonon DOS going from a bulk crystal to a nanoparticle is likely to have observable experimental effects. In the following sections, we take note of experiments that have, or have not, revealed such effects.

### Effect of the Phonon DOS on the Establishment of Thermal Equilibrium

Following absorption of a photon, a luminescent ion generally relaxes to a state of quasi-thermal equilibrium; an excited state in which the electronic and vibrational levels are populated according to properly weighted Boltzmann factors. The relaxation to equilibrium requires the participation of all phonon modes as well as the mixing of those modes, and generally occurs on a picosecond timescale. For small particles, where the low frequency modes are discrete and well separated from one another, we may expect the establishment thermal equilibrium following excitation to be inhibited.

Experimental evidence of this effect has been observed by G. Liu et al.,<sup>20,21</sup> who conducted emission and excitation experiments on Er-doped Y<sub>2</sub>O<sub>3</sub> nanoparticles with radii  $\sim 400$  nm and 25 nm. Figure 8 shows an emission spectrum at 3 K of the  $^4S_{3/2} \rightarrow ^4I_{15/2}$  transition of Er in Y<sub>2</sub>O<sub>3</sub> following excitation with a pulsed laser into the  $^4F_{3/2}$  level. In the 400 nm particles, the emission originates from only the lowest energy level (level (a) in Figure 8) of the  $^4S_{3/2}$  manifold, because in thermal equilibrium at 3 K only the lowest level of the  $^4S_{3/2}$  manifold is occupied. In the 25 nm nanoparticles, however, one observed anomalous hot emission bands that originate from the upper crystal field level (level (b) in Figure 8) of the  $^4S_{3/2}$  manifold.

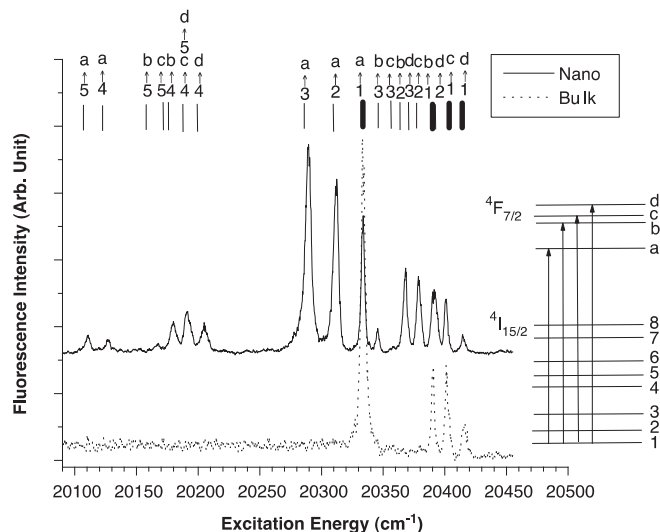


**Figure 9.** Excitation spectra of the  $^7F_2$  to  $^4I_{15/2}$  emission in bulk (dotted line) and in nanocrystals (solid line) of Er:Y<sub>2</sub>O<sub>2</sub>S at 2.6 K.<sup>20</sup>

The data suggest that in the 400 nm particles there is fast relaxation from level (b) of the  $^4S_{3/2}$  manifold to its lower level (a), leading to emission only from the lower  $^4S_{3/2}$  level. In the 25 nm nanoparticles, however, this relaxation from (b) to (a) is inhibited, since there is no available mode to accept a phonon of that low frequency ( $\sim 15$  cm<sup>-1</sup>). Consequently, the one-phonon decay process at that energy does not occur in the nanoparticle, allowing level (b) to remain populated long enough to emit a photon.

Anomalous bands were also observed by Liu et al. in excitation spectra of the same system (Figure 9). In the larger particles (dotted line) at low temperature, the excitation spectrum shows four absorption transitions (1  $\rightarrow$  a, b, c, d) that lead to emission. This behavior is completely unsurprising, since only the lowest energy level is occupied before excitation. In the nanocrystals (solid line), however, the excitation spectrum shows numerous lines in addition to the four lines observed in the bulk spectrum. An analysis of these lines shows that they represent transitions from crystal field levels 1–5 of the ground  $^4I_{15/2}$  manifold to the crystal field levels a - d of the excited  $^4F_{7/2}$  manifold, as shown in the insert of Figure 9. This is rather surprising, since thermal equilibrium demands that only the lowest energy level be occupied at  $T = 2.6$  K.

The results shown in Figure 9 are explained as follows. In the excitation experiment, absorption of the exciting laser light into the  $^4F_{7/2}$  level is followed by a fast relaxation to the lower  $^4S_{3/2}$  level. This relaxation, which is accompanied by the emission of phonons, is fast enough to occur before the laser pulse has ended. These phonons created during relaxation may be absorbed by a nearby Er ion, causing that Er ion to become excited to one of the excited levels in the ground state manifold. This is done either via a direct one-phonon process or via two phonon processes, namely Orbach or Raman processes. Once in the upper levels of the  $^4I_{15/2}$  ground state manifold, relaxation to nearby lower levels becomes improbable due to the absence of phonon modes at the required (low) energies for relaxation. As the laser pulse continues, absorption from the now occupied higher levels of the  $^4I_{15/2}$  manifold to the  $^4F_{3/2}$  levels results in the hot bands in Figure 9. We note that at  $\sim 7$  K, these hot bands disappear. Apparently, even at 7 K, two-phonon processes are fast enough for thermal equilibrium to be established on a sub-ns timescale.

These results demonstrate the effect of the discreteness of the phonon DOS in small particles. However, they also hint that observing such effects may be difficult; the discreteness of the phonon DOS can be masked by second-order processes and/or by the mixing of phonons due to anharmonic contributions to the potential, even at low temperatures.

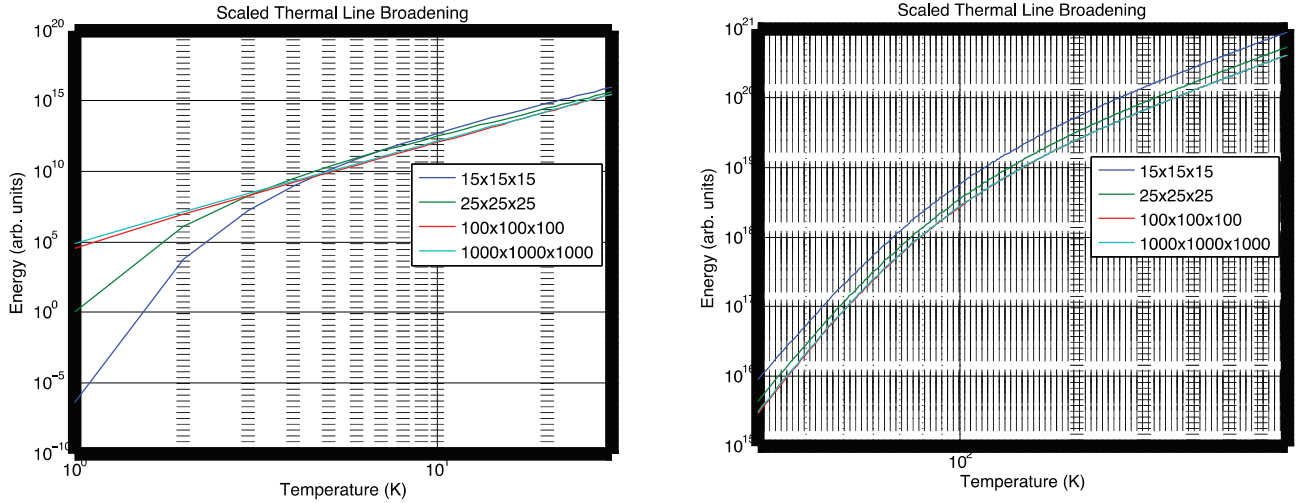


**Figure 10.** Temperature dependence on the thermal broadening of a spectral line (given by the sum in Equation 48) for cubic nanoparticles ( $15 \times 15 \times 15$ -black,  $25 \times 25 \times 25$ -blue,  $100 \times 100 \times 100$ -red,  $1000 \times 1000 \times 1000$ -green) for temperatures ranges 1–30 K and 30–700 K.

### Thermal Broadening and Shifting of Sharp Spectral Lines in Nanoparticles

*Broadening of a spectral line in a nanoparticle.*— In Thermal broadening and shifting of sharp spectral lines section, the broadening of a spectral line was found to depend on the phonon DOS and on the phonon occupation number of each state. Earlier, we estimated the phonon density of states using Debye approximation, and the sum over all phonon states was carried out by integration. For nanoparticles, the phonon DOS is a discrete function of phonon frequency, and the sum over states must be carried out directly.

As discussed earlier, the thermal broadening of a spectral line is mainly due to the Raman scattering of phonons. The rate of such processes involving the absorption of a phonon from  $k$  and an emission of a phonon into mode  $k'$  is given by Equation 27:

$$(W_{Raman})_{kk'} = \frac{2\pi}{\hbar^2} |\alpha'|^2 \omega_k \omega_{k'} n_k (n_{k'} + 1) \varrho(\omega_f), \quad [44]$$

where  $\alpha'$  is given by 26. The total transition rate is found by summing 44 over all final states of the lattice, subject to the condition that energy must be conserved. In nanoparticles, the phonon DOS,  $\varrho_{nano}(\omega)$ , depends on the size and shape of the sample. Examples are shown in Figure 6. In describing the density of phonon states, it is important to recall that each phonon mode represents a resonance of the solid, having a peak, line shape ( $f(\omega)$ ), and line width ( $\Delta\omega$ ). The phonon DOS evaluated at frequency  $\omega_i$  is

$$\varrho_{nano}(\omega_i) = g(\omega_i) f(\omega_i), \quad [45]$$

where  $g(\omega_i)$  is the degeneracy modes at frequency  $\omega_i$ . Though the line shape is more correctly represented as a Lorentzian, we shall simplify the shape to the “top hat” function, that is:

$$f(\omega) = \begin{cases} 1/\Delta\omega & \text{for } \omega - \Delta\omega/2 \leq \omega \leq \omega + \Delta\omega/2 \\ 0 & \text{elsewhere} \end{cases}, \quad [46]$$

We also assume that linewidth of each resonance,  $\Delta\omega$ , independent of  $\omega$ . For sharp spectral lines, we further assume that the main contribution to the broadening occurs when  $|\omega_k - \omega_{k'}| \leq \Delta\omega/2$ , that is, the phonons in the scattering process are of nearly the same frequency. In such a scheme, we may approximate the density of final states as

$$\varrho(\omega_f) = \varrho_{nano}(\omega_i) \varrho_{nano}(\omega_i') \Delta\omega_i \Delta\omega_i' \delta(\omega_i - \omega_i') = \varrho_{nano}^2(\omega_i) (\Delta\omega)^2 \quad [47]$$

Summing 44 over phonon frequencies, and using Equations 45–47, the total transition rate of the Raman process is

$$\begin{aligned} W_{Raman} &= \frac{2\pi}{\hbar^2} |\alpha'|^2 \sum_k g^2(\omega_k) \omega_k^2 n_k (n_k + 1) f^2(\omega_k) (\Delta\omega)^2 \\ &= \frac{2\pi}{\hbar^2} |\alpha'|^2 \sum_k g^2(\omega_k) \omega_k^2 n_k (n_k + 1) \end{aligned} \quad [48]$$

The degeneracy term  $g(\omega)$  includes all modes within a range  $\omega \pm \Delta\omega/2$ . In Figure 6, the energy axis is broken up into 1000 bins, each with energy range  $\Delta\omega \sim 0.5 \text{ cm}^{-1}$ .  $g(\omega_k)$  is given by the number of modes in the  $k^{\text{th}}$  bin, where  $\omega_k$  is the central frequency of the bin. The term  $n_k$  carries the temperature dependence of the broadening. The sum expressed in 48 was carried out for four particle sizes and over a range of temperatures from 1 K to 700 K. The results are shown in Figure 10. The vertical axis in Figure 10 is in arbitrary units, so the curves show only the temperature dependence of the broadening. We make the following observations regarding these results.

1. The strongest temperature dependence of the line broadening occurs at temperatures below 10 K independent of particle size. The temperature dependence is stronger for smaller particles in this temperature range.
2. Above 300 K the curvature of the lines in Figure 10 are independent of particle size, indicating that the thermal dependence of the broadening is the same for all particle sizes.
3. Figure 10 also shows that above  $\sim 10$  K the absolute broadening to be larger for smaller particle sizes. However, this effect depends on the details of the calculation (e.g. the binning of the data and the “top hat” line shape function), and should not be taken too seriously.

To understand the strong temperature dependence of the broadening at low temperatures, it is useful to consider not just the phonon density of states, but also the occupancies of the phonon modes. Figure 11 shows the product  $\varrho_{nano}(\epsilon)n(\epsilon)$  for the 3 nm particle at  $T = 10$  K, 100 K, and 500 K. At 10 K, only a few modes are occupied, and the phonon occupation numbers are very small, much less than 1. At 1 K, the occupancy of the lowest mode in the 3 nm particle is  $\sim 10^{-23}$ . Thus, in a nanoparticle, there are essentially no phonons at 1 K, so there is no broadening. This helps explain the strong dependence (on a logarithmic scale) of the broadening in the 3 nm particles at low temperature shown in Figure 10.

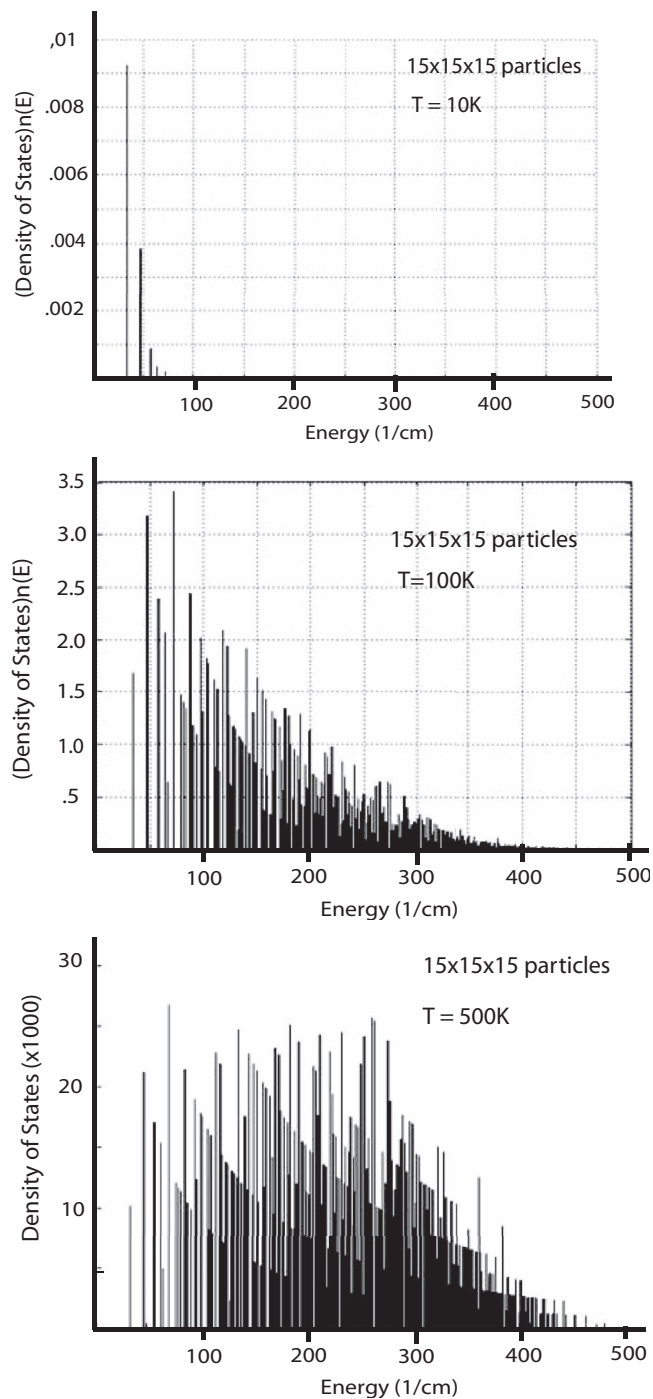


**Figure 11.** Graphs showing the number of phonons as a function of phonon energy, i.e.  $g(\epsilon)n(\epsilon)$  vs.  $\epsilon$ , for cubic nanoparticles  $15 \times 15 \times 15$  atoms (size  $\sim 3$  nm) at  $T = 10, 100,$  and  $500$  K.

Using hole-burning experiments, Meltzer and Hong<sup>22</sup> examined the broadening of the  ${}^7F_0 \rightarrow {}^5D_0$  transition of  $\text{Eu}_2\text{O}_3$  spherical nanoparticles of different diameters (5.4, 7.6, and 11.6 nm) at temperatures between 4 K and 10 K. They observed a  $T^n$  dependence, where  $3 < n < 4$ , for the thermal broadening of the line. This dependence is much smaller than that shown in Figure 10 for the 5 nm particles, and was also much smaller than their own calculated predictions. In contradiction to the results in Figure 10, the authors observed the thermal broadening increasing as the particle size decreases. To explain this they refer to calculations that posit an inverse relation between the electron-phonon coupling and particle size.<sup>23</sup>

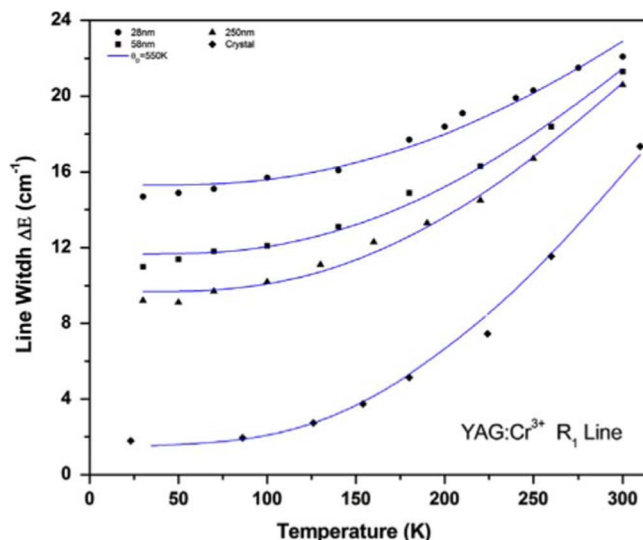


**Figure 12.** Linewidth vs. temperature of the  $R_1$  line in nanopowders ( $\bullet$ , 28 nm,  $\blacksquare$ , 58 nm,  $\blacktriangle$ , 250 nm), and in a single crystal ( $\blacklozenge$ ) of Cr-doped YAG. The solid lines are fits to Equation 33.

Erdem et al.<sup>24</sup> measured the linewidth of the  ${}^2E \rightarrow {}^4A_2$  transition of Cr-doped YAG nanoparticles at temperatures from 30 K to 300 K as a function of particle size (Figure 12). The results were fit to Equation 34 assuming Debye temperature of 550 K and where the electron-phonon coupling parameter,  $\alpha'$ , was allowed to vary. The fits to equation (64) are reasonable good, showing that even in nanoparticles as small as 28 nm behave similar to the bulk crystal. This is consistent with the behavior shown in Figure 10. Excellent fits to Equation 34 were also reported by Bilir et al. on the temperature dependence of the linewidth of Nd nanoparticles ranging in diameters from 16 to 250 nm.<sup>25</sup>

It is interesting to note that in two of the above works<sup>24,25</sup> the data indicate that the thermal broadening decreases as the particle size decreases. The authors suggested this was due to the fact that the electron-phonon coupling parameter decreases with particle size. They explain this result as follows: ions near the surface have bond lengths with neighbors that are slightly above the standard length, which would decrease the overlap of the wavefunctions of the ion and those of its ligands, thereby lowering the electron-phonon interaction. This explanation is consistent with arguments that the electron-phonon coupling depends on the covalency of ion-ligand bond, as covalent bonds tend to have greater overlap between the wavefunctions of the electrons associated with the ions with those of the ligands.<sup>17-19,26</sup> In Reference 22, on the other hand, the authors measured the broadening of  $\text{Mn}^{2+}$  in ZnS nanoparticles of various sizes, and concluded that particle size has no effect on the electron-phonon coupling.

The examples above show an unresolved conflict in the behavior of the electron-phonon coupling as the particle size changes. Whereas Meltzer et al.<sup>22</sup> suggest an increase in the coupling as the particle size decreases, the data from Erdem et al.<sup>24</sup> and Bilir et al.<sup>25</sup> suggest a decrease in the coupling as particle size decreases. And finally Suyver et al.<sup>26</sup> conclude that electron-phonon coupling is independent of particle size. Of course, the above works were done in different temperature regimes (4–10 K, 30–300 K, 30–700 K, 4–300 K for Refs. 22–25, respectively), with particles of different sizes, and for weakly-coupled<sup>22-25</sup> and strongly-coupled<sup>25</sup> systems, so the conclusions are not necessarily in conflict with one another. A definitive answer as to how the electron-phonon coupling depends on particle size remains elusive.

*Shifting of a sharp spectral line in a nanoparticle.*— The theoretical treatment of the thermal shift of the energy of the spectral line in a nanoparticle begins with Equation 38 the shift due to a particular

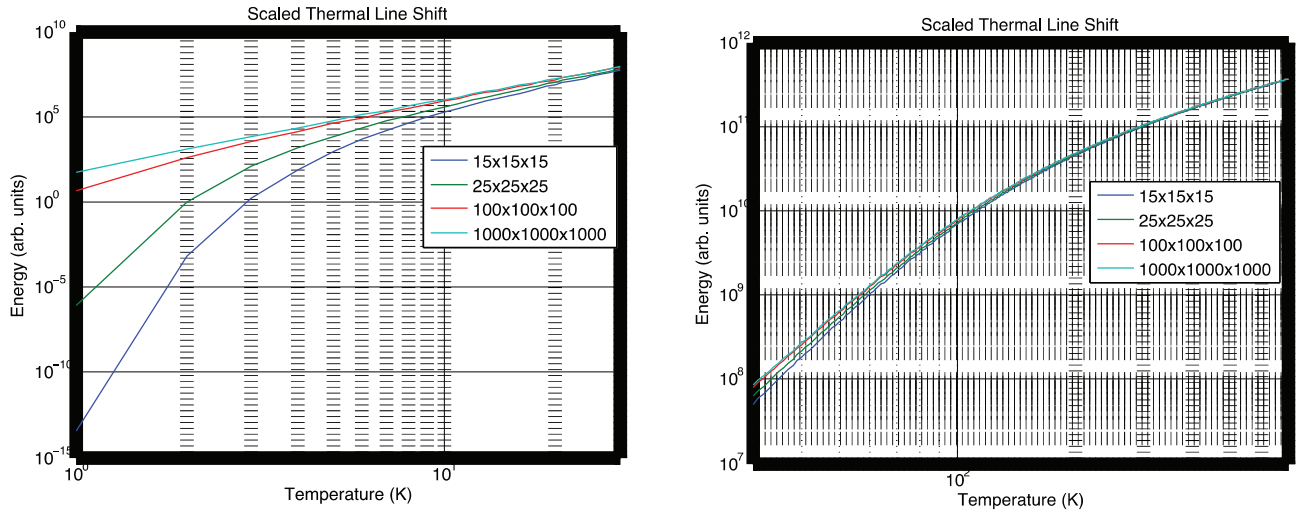


**Figure 13.** Temperature dependence on the thermal shift of a spectral line (given by the sum in Equation 50 for cubic nanoparticles ( $15 \times 15 \times 15$ -black,  $25 \times 25 \times 25$ -blue,  $100 \times 100 \times 100$ -red,  $1000 \times 1000 \times 1000$ -green) for temperatures ranges 1–30 K and 30–700 K.

phonon mode,  $k$ .

$$\Delta\epsilon_k = \frac{\hbar}{Mv_s^2} \left[ \langle \phi_i | V_2 | \phi_i \rangle + \sum_j \frac{|\langle \phi_j | V_1 | \phi_j \rangle|^2}{\epsilon_i - \epsilon_j} \right] \omega_k (2n_k + 1) \quad [49]$$

To find the total thermal shift of the particle, we neglect the contribution of spontaneous emission in 49 (i.e.,  $(2n_k + 1)$  becomes  $(2n_k)$ ), and sum 49 over all phonon modes. Referring to 45 and 46, the total thermal shift can be written as:

$$\Delta\epsilon = \frac{2\hbar}{Mv_s^2} \left[ \langle \phi_i | V_2 | \phi_i \rangle + \sum_j \frac{|\langle \phi_j | V_1 | \phi_j \rangle|^2}{\epsilon_i - \epsilon_j} \right] \sum_k g(\omega_k) \omega_k n_k \quad [50]$$

The sum in 50 carries the temperature dependence of the thermal line shift. Figure 13 shows the values of the sum in Equation 50 for cubic nanoparticles ( $15 \times 15 \times 15$ ,  $25 \times 25 \times 25$ ,  $100 \times 100 \times 100$ , and  $1000 \times 1000 \times 1000$  atoms) at temperatures between 1 K and 700 K. Similar to the case of line broadening, the main differences between the shift in large and small particles occurs at very low temperatures. At high temperatures, the thermal shift is nearly independent of particle size.

Erdem et al. studied the lineshift of the  ${}^2E \rightarrow {}^4A_2$  emission line of  $\text{Cr}^{3+}$  in YAG in nanoparticles and in a bulk crystal, and the results are shown in Figure 14.<sup>24</sup> The results show that the thermal lineshift decreases as the particle size decreases. In that work, the lineshift was fit to Equation 39 assuming a Debye temperature of 550 K, and it was found that, as with the thermal line broadening data, the electron-phonon coupling parameter decreased with particle size. Given the lack of a comprehensive theory and the dearth of experimental data on the dependence of the line shift on particle size, more work is required to say definitively why the shift is less in smaller particles.

### Vibronic Transitions

Following excitation, the decay of an isolated ion can occur via (1) emission of a photon, (2) emission of phonon(s), or (3) the emission of a photon concurrent with the absorption or emission of one or more phonons. This third process is referred to as a vibronic transition. For broad-band emitters, these transitions are the dominant feature in both absorption and in emission, whereas for sharp line emitters, the vibronic transitions appear as sidebands to the zero-phonon line. Figure 15 shows spectra of Cr-doped GGG, which produces both broad band and sharp line emissions at high temperatures. At low temperatures, this system shows a sharp zero-phonon line, with highly

structured sidebands, with no broad band emission. This type of emission, i.e., sidebands and a dominant zero-phonon line, is common to most optically active ions that are weakly-coupled to the lattice. Vibronic sidebands in weakly-coupled systems have been discussed

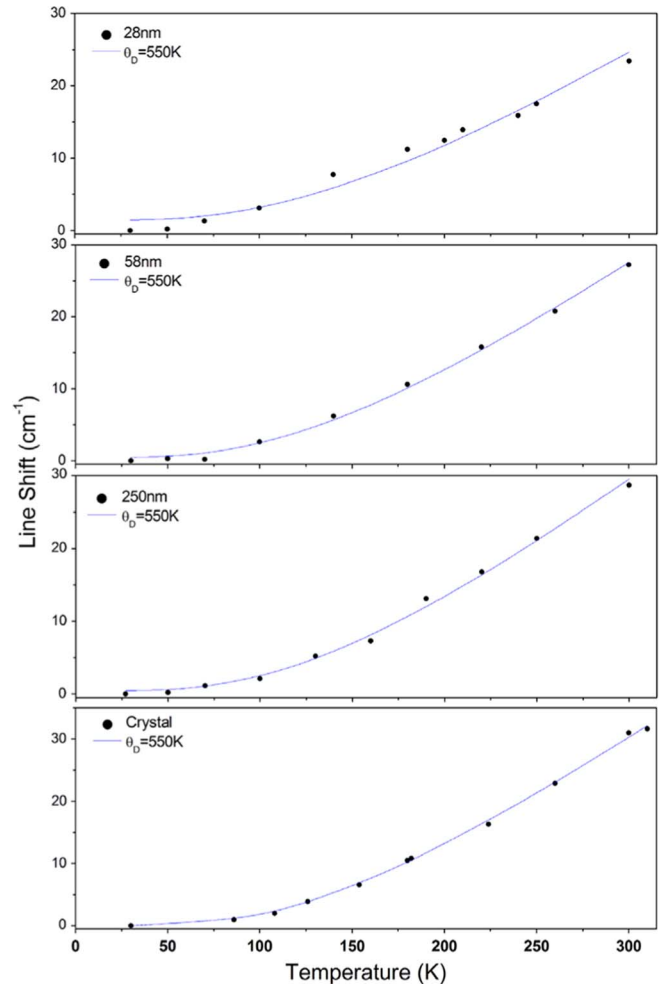


**Figure 14.** Line shift vs. temperature of the  $R_1$  line from Cr-doped YAG nanopowders and from a single crystal. The blue lines are fits to Equation 39.

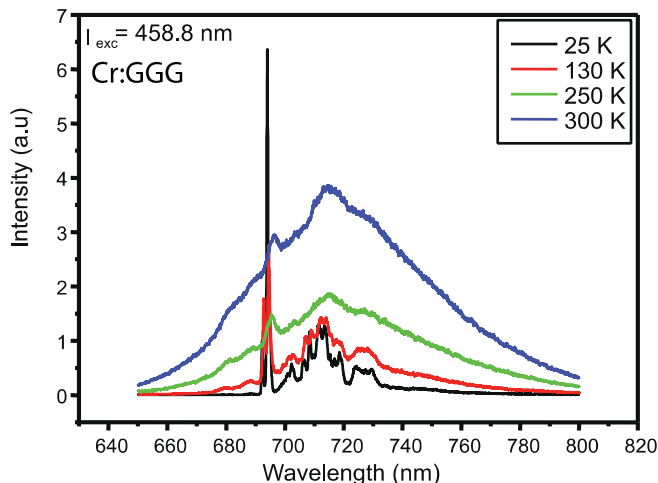


**Figure 15.** Emission spectra of  $\text{Cr}^{3+}$  in GGG. At low temperatures the emission is dominated by the R-lines (originating from the  ${}^2E$  level) and the vibronic sideband. As temperature increases, a broad band emission from the  $\text{Cr } {}^4T_2$  level is also observed.

by several workers [e.g. 27–29]. In this section we focus on vibronic transitions in such weakly-coupled systems.

*Vibronic sidebands of sharp lines - Theory.*— In this section we review some theoretical aspects of vibronic transitions in the weak coupling limit. In such systems, the narrow zero-phonon line is accompanied by sidebands, which result from the modulation of the zero-phonon transition by the vibrations of the solid. In the low temperature spectrum shown in Figure 15, one immediately notices the rich structure contained in that sideband, structure that contains information of the phonon density of states. To explain such a structure, we must consider the interaction of the ion with the various phonon modes of the crystal.

The transition rate of a vibronic transition involving the emission of a photon and of a phonon in the  $k^{\text{th}}$  mode is governed by terms having the following form:

$$W_k \propto [|\langle \phi_f n_{k+1} | O_{ph} | \phi_j n_k \rangle \langle \phi_j n_k | O_{rad} | \phi_i n_k \rangle|^2 + |\langle \phi_f n_{k+1} | O_{rad} | \phi_j n_k \rangle \langle \phi_j n_{k+1} | O_{ph} | \phi_i n_k \rangle|^2] \quad [51]$$

where  $O_{rad}$  and  $O_{ph}$  in Equation 51 represent the appropriate radiative and nonradiative operators and  $\phi_i$ ,  $\phi_j$ , and  $\phi_f$  are the wavefunctions of the initial, intermediate and final electronic states, respectively. The first term in Equation 51 represents a process whereby a photon is created in a transition from the initial electronic state to an intermediate electronic state, and then a phonon is emitted in the transition to the final electronic state. The second term reverses the order of these transitions. Figure 16 shows a schematic drawing of a vibronic transition that represents by the second term in Equation 51.

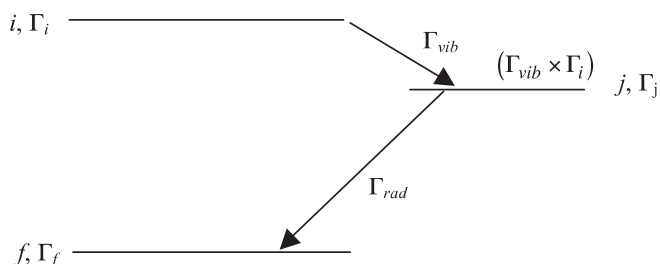


**Figure 16.** The vibronic emission process with states and transition operators labeled according to irreducible representations.

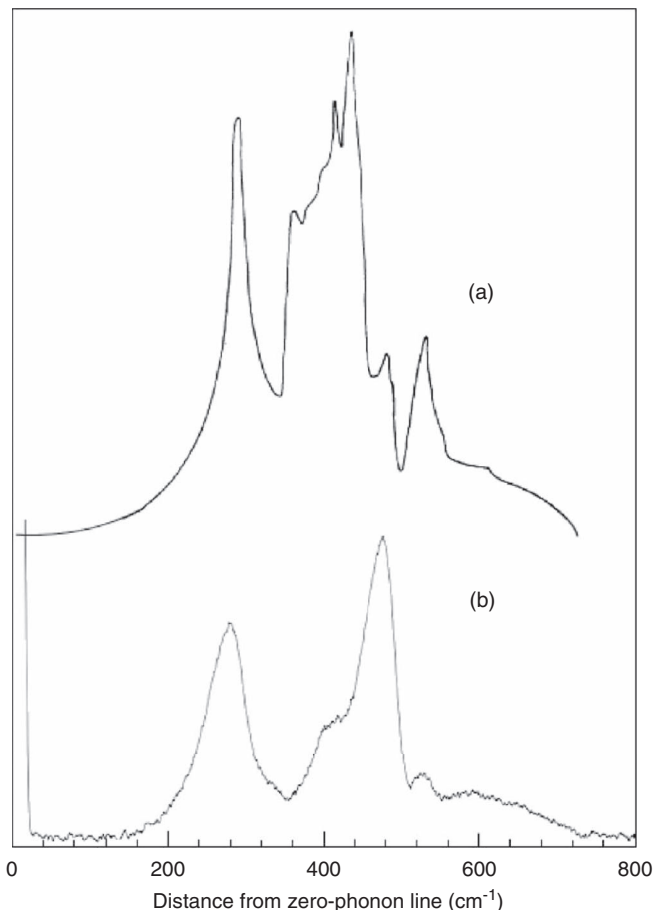


**Figure 17.** (a) The density of states of MgO as determined from neutron scattering<sup>31</sup> shown with (b) the vibronic sideband of  $\text{MgO:V}^{2+}$ .<sup>29</sup>

Each of the electronic wavefunctions and the operators have a certain symmetry, and using group theory one can associate them with certain irreducible representations. We make the following definitions.

- $\Gamma_i$ : the irreducible representation of the initial electronic state of the transition
- $\Gamma_f$ : the irreducible representation of the final electronic state of the transition
- $\Gamma_r$ : the irreducible representation of the radiative operator (We will assume that this is the electric dipole operator.)
- $\Gamma_v$ : the irreducible representation of the vibrational mode involved in the transition

The selection rule for the vibronic transition, shown in Figure 16, is that the direct product  $\Gamma_i \times \Gamma_{vib} \times \Gamma_r$  must contain  $\Gamma_f$ . That is

$$\Gamma_f \in \Gamma_i \times \Gamma_v \times \Gamma_r \quad [52]$$

We note that 52 is merely a selection rule, and can only be used to determine if a particular transition can occur; it cannot be used to determine the strength of a transition.

*Vibronic sidebands of sharp lines - Experimental.*— Consider the case of a vibronic spectrum in emission at low temperature of  $\text{MgO:V}^{2+}$ , shown in Figure 17b.<sup>29</sup>  $\text{V}^{2+}$  is a  $d^3$  ion surrounded by six oxygen ions in octahedral symmetry. Because the site has inversion symmetry, electric dipole transitions between two electronic states within the  $d^3$  configuration are forbidden. As a result, the purely radiative transitions (accounting for the zero-phonon line) are driven by the magnetic dipole operator. Odd vibrations of the local complex destroy this inversion symmetry, so that the vibronic transitions involving such vibrations are electric dipole allowed.

Applying Equation 52 to the case of vibronic transitions in  $\text{MgO}:\text{V}^{2+}$ , it is possible to determine which vibrations can contribute to the observed phonon sideband. First, we observe that the normal vibrational modes of the site symmetry of the octahedral group  $O_h$  are either purely even or purely odd. The representation of the final electronic state ( $\Gamma_f$ ) of the  $\text{V}^{2+}$  ion is known to be even. Since the electric dipole operator ( $\Gamma_{rad}$ ) is odd, then a transition from the intermediate state via the electric dipole, according to Equation 52, will be allowed only if the intermediate state is odd. The initial (excited) electronic state of  $\text{V}^{2+}$  ( $\Gamma_i$ ) is also even, so that only odd vibrations will be involved in the transition from  $\Gamma_i$  to  $\Gamma_j$ . Thus, Equation 52 reduces to a statement of the parity selection rule.

It has been shown that of the phonons modes featured most prominently in the density of states of  $\text{MgO}$ , most of them can induce the octahedral complex to oscillate in one or more of its odd vibrational modes.<sup>30</sup> As a result, nearly all of the crystal phonon modes are able to participate in the vibronic transitions. The phonon spectrum of the  $\text{MgO}$  crystal (obtained by neutron scattering data)<sup>31</sup> is shown in Figure 17a. The similarity of the shape of the low temperature vibronic sideband (Figure 17b) to that of the phonon spectrum is striking, and suggests that the vibronic sideband can be closely related to the phonon spectrum of the lattice. That these two spectra show striking similarities and that nearly all phonon modes of the  $\text{MgO}$  crystal can cause local vibrations to participate in the transition is not coincidental. However, proving that there is a one-to-one correspondence between the peaks (and valleys) of the two spectra is not trivial, since that would require calculating the transition probabilities for each of the 3N-6 normal modes of the crystal. Even if such a calculation could be done, it is no guarantee that such a calculation would be able to reproduce the observed vibronic spectrum. Generally speaking, the shape of the vibronic spectrum will not exactly mimic that of the density of phonon states. It may, however, be a practical way of gaining insight into the phonon density of states for some crystals.

The above observations suggest that in small nanocrystals, where the confinement on the density of states is most severe, one would expect that changes to the density of states to be obvious in the vibronic spectrum of the nanoparticle. In fact, such a result would represent perhaps the most direct experimental evidence of the reduced density of states in nanoparticles. Unfortunately, because of surface effects, there is a significant amount of disorder in a nanoparticle, resulting in a broadening of the zero-phonon line (and of the vibronic sidebands). The sum of the contributions from various sites overlaps with a large portion of the phonon sidebands of the zero phonon line from the "normal" site. An example of this is shown in the vibronic spectra of Cr-doped YAG nanoparticles shown in Figure 18. Perhaps due to the fact that this overlap is most prominent near in the low energy range of the sidebands, where the most obvious changes (i.e., discreteness of the density of states and absence of the very low energy modes) to the density of states occur, there is no reported vibronic spectrum that clearly shows the vibronic spectrum changing with particle size. The difficulty in observing this is also complicated by the fact that the emission from nanoparticles is often very weak, probably because of the large number of surface states.

### Energy Transfer Among Ions in Nanoparticles

In the context of optically active ions in solids, energy transfer refers to an excited ion transferring all or part of its electronic energy non-radiatively to another ion. A theoretical treatment of this process was first developed by Förster<sup>32</sup> and Dexter.<sup>33</sup> Though energy transfer is known to occur between a variety of different ions, we focus here on energy transfer among like ions.

When like ions reside in identical sites in a lattice, energy transfer will be a resonant process, and can be very efficient if the ion-ion distance is short enough. As the concentration of the dopant increases, the average ion-ion distance decreases and the probability per unit time of energy transfer increases, and the excited electronic energy can migrate through the lattice. In an ideal lattice (i.e. one with no defects) such an energy transfer process, no matter how fast, will not affect

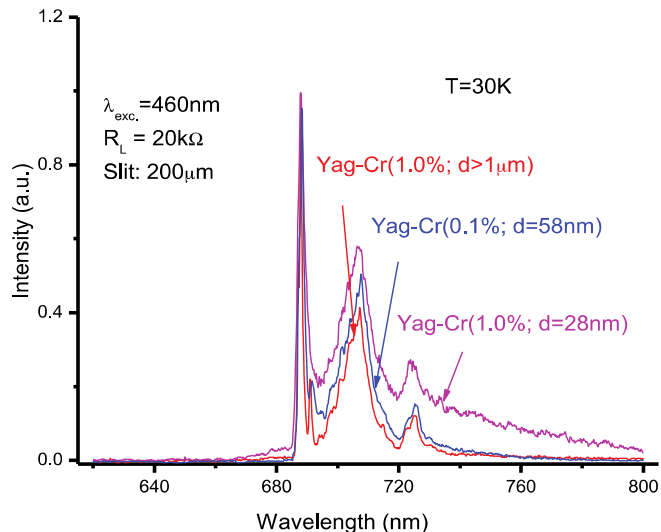


**Figure 18.** Emission spectra at different temperatures of Cr:YAG particles of 28 nm, 58 nm, and >1000 nm. Notice the broadening of the spectral lines and an enhanced background signal as the particle size decreases.

the luminescence properties of the system. However, defects are always present in the lattice, and energy transfer from an excited ion to a defect is possible. When the energy transfer becomes very fast the excitation energy migrates rapidly through the lattice until it reaches a defect site, at which point the energy is lost. This is represented schematically in Figure 19. In such a system, increasing the concentration of the dopant ion has two effects on the luminescence properties of the crystal: (1) a decrease in the luminescence intensity, and (2) a decrease of the excited state lifetime of the dopant ion. The defect sites are sometimes referred to as killer sites. The decrease in the luminescence as concentration of dopant ions increases is referred to as a *concentration quenching*.

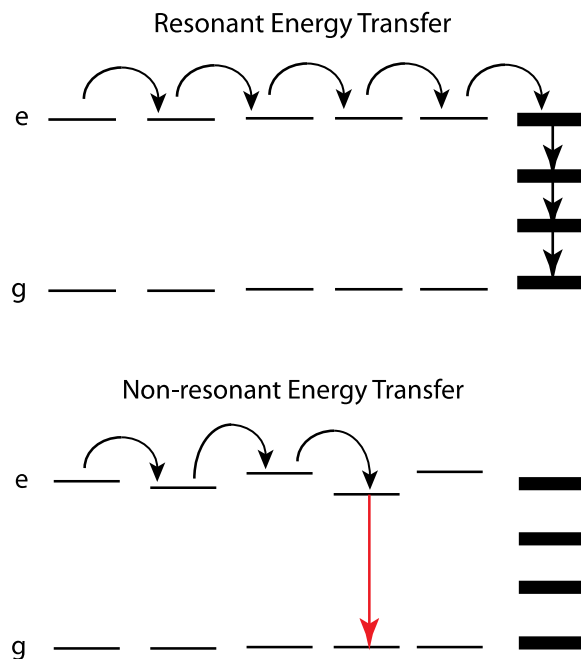


**Figure 19.** Schematics showing energy transfer among like ions. The resonant case is typical for bulk materials, and the non-resonant case is more common to small nanoparticles, where disorder due to surface effects are responsible for the lack of resonance.

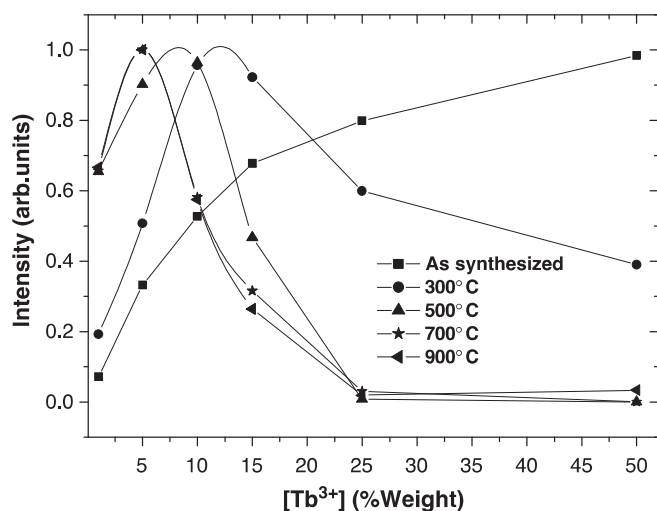


**Figure 20.** A plot of the luminescence intensity from Tb-doped  $Y_2O_3$  nanoparticles of different sizes.<sup>39</sup> (Average particle sizes: 3 nm – as synthesized, 6 nm - 300°C, 21 nm - 500°C, 35 nm - 700°C, 58 nm - 900°C.) Note that the curves are normalized so that the maximum emission intensity from each sample is set to unity.

Now let us consider what happens in a nanoparticle. In the core of the nanoparticle, the ions are located at sites that are nearly identical to sites in the bulk. As one moves closer to the surface, however, these sites become slightly distorted, and as a result the energy levels of the ions shift, becoming out of resonance with those at the core. Energy transfer between two ions that are not in resonance requires the emission or absorption of one or more phonons to make up the energy difference. The probability per unit time of this *phonon-assisted* energy transfer due to the participation of modes with frequency  $\omega_k$  is given by:<sup>34</sup>

$$W_k = \frac{2\pi b}{v_s V} \left( \frac{R_0}{R} \right)^{s-2} \omega_k Q(\omega_k) \{ n(\omega_k) + 1 \} n(\omega_k), \quad [53]$$

where  $s$  is the order of the multipole interaction ( $s = 6$  for dipole-dipole interaction),  $V$  is the volume of the nanoparticle,  $b$  contains to the coupling between the two ions and the electron-phonon coupling, and  $\hbar\omega_k$  is of the correct energy to make up for the energy mismatch between the two excited levels. The terms in the curly bracket in 53 contain the temperature dependence of the transfer rate, with top term applying to phonon emission and the bottom term to phonon absorption.

As shown in Figure 20, in the case of resonant energy transfer the energy is finally lost at a killer site, while in the non-resonant case, the migration of energy is inhibited, and the energy may be given off as luminescence.

In typical bulk crystals, the concentration quenching of luminescence appears at dopant concentrations of approximately molar 1%. As the concentration continues to increase, the total luminescence from the crystal decreases. When the dopant level reaches several molar percent (eg. 10 - 20%) the luminescence becomes difficult to detect, having decreased by a few orders of magnitude. In basically all bulk materials, the amount of luminescence efficiency at high dopant concentrations continues to decrease as the concentration is further increased.

In nanoparticles, several groups have found that the luminescence in nanoparticles persists at higher dopant concentrations than in bulk materials,<sup>35-38</sup> and sometimes even increases with increasing dopant concentration. Figure 20 shows the example of a Tb-doped  $Y_2O_3$  system in which for the smallest particles the luminescence continues to increase at concentrations far higher than for the much larger particles.<sup>39</sup> For the largest sized particles, the luminescence intensity drops precipitously at concentrations above  $\sim 5\%$ , whereas for the 3 nm (“as synthesized”) particles the luminescence intensity is still

increasing even at concentration of 50%. This is explained as being due to the fact that as the nanoparticles decrease in size, the ions become more and more out of resonance with one another, making energy transfer less probable. Also, given that the phonon DOS term in 53 becomes a highly discrete function for 3 nm particles, it is likely that phonon modes present in the bulk that participate in the energy transfer process are not available in the nanoparticles. Thus, the probability of energy transfer as particles size is decreased becomes smaller for two reasons: (1) greater disorder leads to greater nonresonance between ions, and (2) the reduced availability of phonon modes to participate in the energy transfer process.<sup>34</sup>

## Conclusions

This paper presented some theoretical treatments of some non-radiative processes that affect the luminescence properties of optically active ions in solids, and considered how such properties might be affected as the size of the particles are reduced to the nano-regime. This paper first presented a detailed discussion of the electron-phonon coupling terms for the different adiabatic approximations were then discussed. This electron-phonon coupling was used to determine the thermal broadening and shifting of sharp spectral lines of optically active ions in solids. Integral to the broadening and shifting of spectral lines, and indeed to most non-radiative processes, is the phonon density of states in the system under investigation. Given that one goal of the paper was to examine how non-radiative processes depend on particle size, we then investigated how the phonon density of states depended on particle size. This investigation consisted of calculations of the phonon density of states for cubic nanoparticle, where it was found that for very small particles, the phonon density of states becomes very different than for bulk particles. The most obvious change in the phonon density of states between macro and nano systems occurs at the low energy end of the spectrum. With this background, the question of how non-radiative processes in doped insulators are altered as the size of the particles change from macroscopic to nano-sized was considered.

The fact that the electronic states of optically active ions in insulators are highly localized to the site of the ion, the general theory of non-radiative transitions is largely unaltered as the particle size changes. A review of the theory of thermal line broadening and line shifting, presented early in the paper, allowed us to determine exactly at what point the traditional theory had to be altered so as to be applied to small particles, this point being where the phonon density of states of the lattice is inserted into the theory. Using the calculated densities of states for cubic nanoparticles, we examined the thermal broadening and shifting of spectral lines for various particle sizes over a wide temperature range. Initial results hint that the effects of particle size on the broadening and shifting of lines are most likely to be observed only at low temperatures and in very small particles. Even in particles on the order of 50 nm, one is unlikely to be able to discern any contribution to these processes due to confinement effects of the phonon density of states. Also discussed were the following (1) how the reduced phonon density of states inhibits the systems ability to reach thermal equilibrium, (2) possible changes in the vibronic sidebands, and (3) how the large surface to volume ratio and the reduced density of phonon states conspire to inhibit phonon-assisted energy transfer, reducing the effect of concentration quenching of luminescence.

## Acknowledgments

The Author thanks Ryan Clair of Wheaton College for the calculations of the density of states of the nanoparticles, and also to Professor Rino DiBartolo of Boston College for his assistance and encouragement. The material presented here was supported in part by the National Science Foundation under grant number 1105907.

## References

1. M. Born and R. Oppenheimer, *Ann. Phys.*, **84**, 457 (1927).
2. M. Born and K. Huang, *Dynamical Theory of Crystal Lattices*, Oxford University Press, 1956.

3. J. C. Slater, *Quantum Theory of Molecules and Solids*, Vol I, McGraw Hill, New York, 1963.
4. B. Henderson and G. Imbusch, *Optical Spectroscopy of Inorganic Solids*, Oxford University Press, 2006.
5. W. Demtröder, *Molecular Physics: Theoretical Principles and Experimental Methods*, Wiley Press, 2005.
6. T. Azumi and K. Matsuzaki, *Photochemistry and Photobiology*, **25**, 315 (1977).
7. C. Ballhausen and A. Hansen, *Am. Rev. Phys. Chem.*, **23**, 15 (1972).
8. B. Di Bartolo, "Interaction of Radiation with Ions in Solids", in *Luminescence of Inorganic Solids*, ed. B. Di Bartolo, Plenum Press, 1976.
9. G. Herzberg, *Electronic Spectra of Polyatomic Molecules*, van Nostrand Press, Amsterdam, 1966.
10. X. Wang, W. M. Dennis, and W. M. Yen, *Phys. Rev. B*, **46**(13), 8168 (1992).
11. W. M. Tobert, W. M. Dennis, and W. M. Yen, *Phys. Rev. Lett.*, **65**(5), 607 (1990).
12. J. Frenkel, *Phys. Rev.*, **37**, 17 (1931).
13. C. W. Struck and W. H. Fonger, *J. Luminescence*, **14**, 253 (1976).
14. C. W. Struck and W. H. Fonger, *J. Luminescence*, **10**, 1 (1975).
15. D. E. McCumber and M. D. Sturge, *J. Appl. Phys.*, **34**, 1682 (1963).
16. B. Di Bartolo and R. Peccei, *Phys. Rev.*, **137**(6A), 1770 (1965).
17. A. Ellens, H. Andres, A. Meijerink, and G. Blasse, *Phys. Rev. B*, **55**(1), 173 (1997).
18. A. Ellens, H. Andres, A. Meijerink, and G. Blasse, *Phys. Rev. B*, **55**(1), 180 (1997).
19. J. Suyver, J. Kelly, and A. Meijerink, *J. Luminescence*, **104**, 187 (2003).
20. G. K. Liu, X. Y. Chen, H. Z. Zhuang, S. Li, and R. S. Niedbala, *J. Solid State Chemistry*, **171**, 123 (2003).
21. G. K. Liu, H. Z. Zhuang, and X. Y. Chen, *Nano Lett.*, **2**, 535 (2002).
22. R. Meltzer and K. Hong, *Phys. Rev. B*, **61**(5), 3396 (2000).
23. T. Takagahara, *J. Luminescence*, **70**, 129 (1996).
24. M. Erdem, G. Ozen, U. Yahsi, and B. DiBartolo, *J. Luminescence*, **158**, 464 (2015).
25. G. Bilir, G. Ozen, J. Collins., and B. Di Bartolo, *Appl. Phys. A*, **115**(1), 263 (2014).
26. A. P. Vink and A. Meijerink, *J. Luminescence*, **87-89**, 601 (2000).
27. T. Miyakawa and D. L. Dexter, *Phys. Rev. B.*, **1**, 2961 (1970).
28. F. Auzel and F. "Multiphonon Interaction of Excited Luminescent Centers in the Weak Coupling Limit: Non-radiative Decay and Multiphonon Sidebands", in *Luminescence of Inorganic Solids*, Plenum Press, ed. B. Di Bartolo, 1978.
29. W. Wall, B. Di Bartolo, J. Collins, and H. Orucu, *J. Luminescence*, **129**(12), 1782 (2009).
30. W. Wall, Ph.D. thesis, Boston College, 1974.
31. M. J. Sangster, G. Peckham, and D. H. Saunderson, *J. Phys. C*, **3**, 1026 (1970).
32. Th. Forster, *Ann. Physik*, **2**, 55 (1948).
33. D. L. Dexter, *J. Chem. Phys.*, **21**, 836 (1953).
34. X. Y. Chen, H. Z. Zhuang, G. K. Liu, and G. K. Chen, *J. Appl. Phys.*, **94**(9), 559 (2003).
35. R. E. Muenchausen, L. G. Jacobsohn, B. L. Bennett, E. A. McKigney, J. F. Smith, J. A. Valdez, and D. W. Cooke, *J. Luminescence*, **126**, 838 (2007).
36. X. Qin, Y. Ju, S. Bernhard, and N. Yao, *J. Mater. Res.*, **20**, 2960 (2005).
37. Z. Wei, L. Sun, C. Liao, and C. Yan, *Appl. Phys. Lett.*, **80**(8), 1447 (2002).
38. G. Bilir, G. Ozen, and B. Di Bartolo, *Optical Materials*, **42**, 281 (2015).
39. M. A. Flores-Gonzalez, G. Ledoux, S. Roux, K. Lebbou, P. Perriat, and O. Tillement, *J. Solid State Chem.*, **178**, 989 (2005).